H. W. Wilson, Jr.
ED31

LMSC-HEC TR D065161

(NASA-CR-178868) VISCOUS FLOW COMPUTATIONS FOR ELLIPTICAL TWO-DUCT VERSION OF THE SSME HOT GAS MANIFOLD Interim Report (Lockheed Missiles and Space Co.) 68 p CSCL 20D
N86-30961
Unclas
G3/34 43384

VISCOUS FLOW COMPUTATIONS FOR ELLIPTICAL TWO-DUCT VERSION OF THE SSME HOT GAS MANIFOLD

Interim Report

7 March 1986

CONTRACT NAS8-36090

Prepared for

NATIONAL AERONAUTICS AND SPACE ADMINISTRATION
MARSHALL SPACE FLIGHT CENTER, AL 35812

by

R.P. Roger

by

Lockheed
Missiles & Space Company, Inc.
Huntsville Engineering Center
4800 Bradford Drive, Huntsville, AL 35807

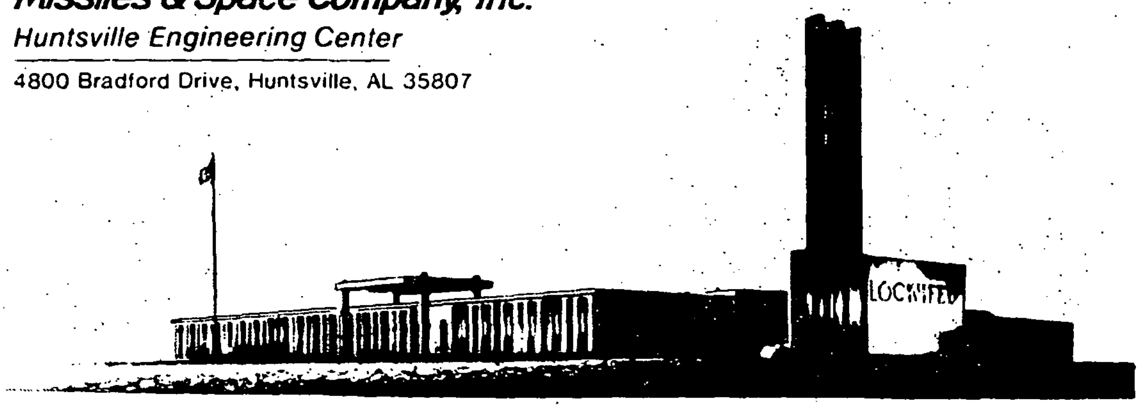

FOREWORD

This report constitutes interim documentation of efforts performed on Contract NAS8-36090 for NASA-Marshall Space Flight Center. It presents results of numerical computations performed by personnel of the Computational Mechanics Group at the Lockheed-Huntsville Engineering Center. The objective was to numerically simulate fluid flow in the experimental Hot Gas Manifold version II$^+$ for the Space Shuttle Main Engine. Both a laminar and a turbulent simulation are presented.

CONTENTS

LIST OF FIGURES

LIST OF FIGURES (Continued)

LIST OF FIGURES (Continued)

LIST OF FIGURES (Concluded)

1. INTRODUCTION

This report presents numerical computation results obtained by personnel of the Computational Mechanics Group at the Lockheed-Huntsville Engineering Center under Contract NAS8-36090. The objective of the effort, as defined by NASA-MSFC, was to numerically simulate viscous subsonic flow in a proposed elliptical two-duct version of the fuel side Hot Gas Manifold (HGM) for the Space Shuttle Main Engine (SSME). The numerical results were to complement both water flow visualization experiments and air flow experiments in the two-duct geometry performed at NASA-MSFC and Rocketdyne.

The three-dimensional character of the HGM consists of two essentially different geometries. The first part of the construction is a concentric shell duct structure which channels the gases from a turbine exit into the second part comprised of two cylindrically shaped transfer ducts. The initial concentric shell portion can be further subdivided into a turnaround section and a bowl section. The turnaround duct (TAD) changes the direction of the mean flow by 180 degrees from a smaller radius to a larger radius duct which discharges into the bowl. The cylindrical transfer ducts are attached to the bowl on one side thus providing a plane of symmetry midway between the two. Figures 1 through 3 will aid in visualizing this geometry. Centerline flow distance from the TAD inlet to the transfer duct exit is approximately two feet.

Details of the approach used to numerically simulate laminar or turbulent flow in that HGM geometry are contained in Section 2. Computational results are presented and discussed in Section 3.

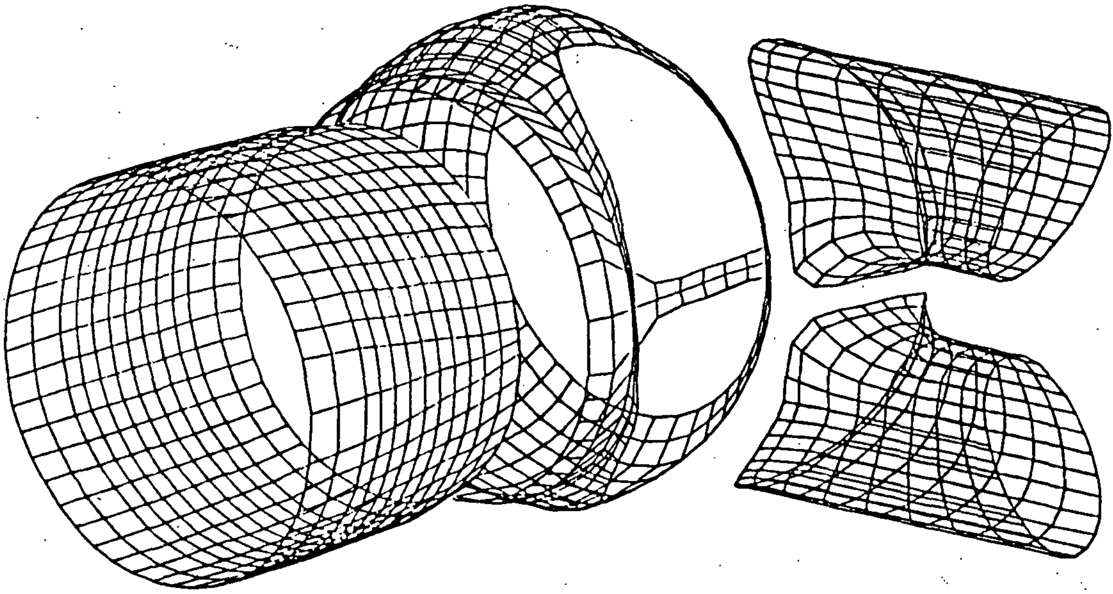

Fig. 1 Sparse Grid Structure of Bowl Inner and Outer Walls and Outer Wall of Transfer Ducts

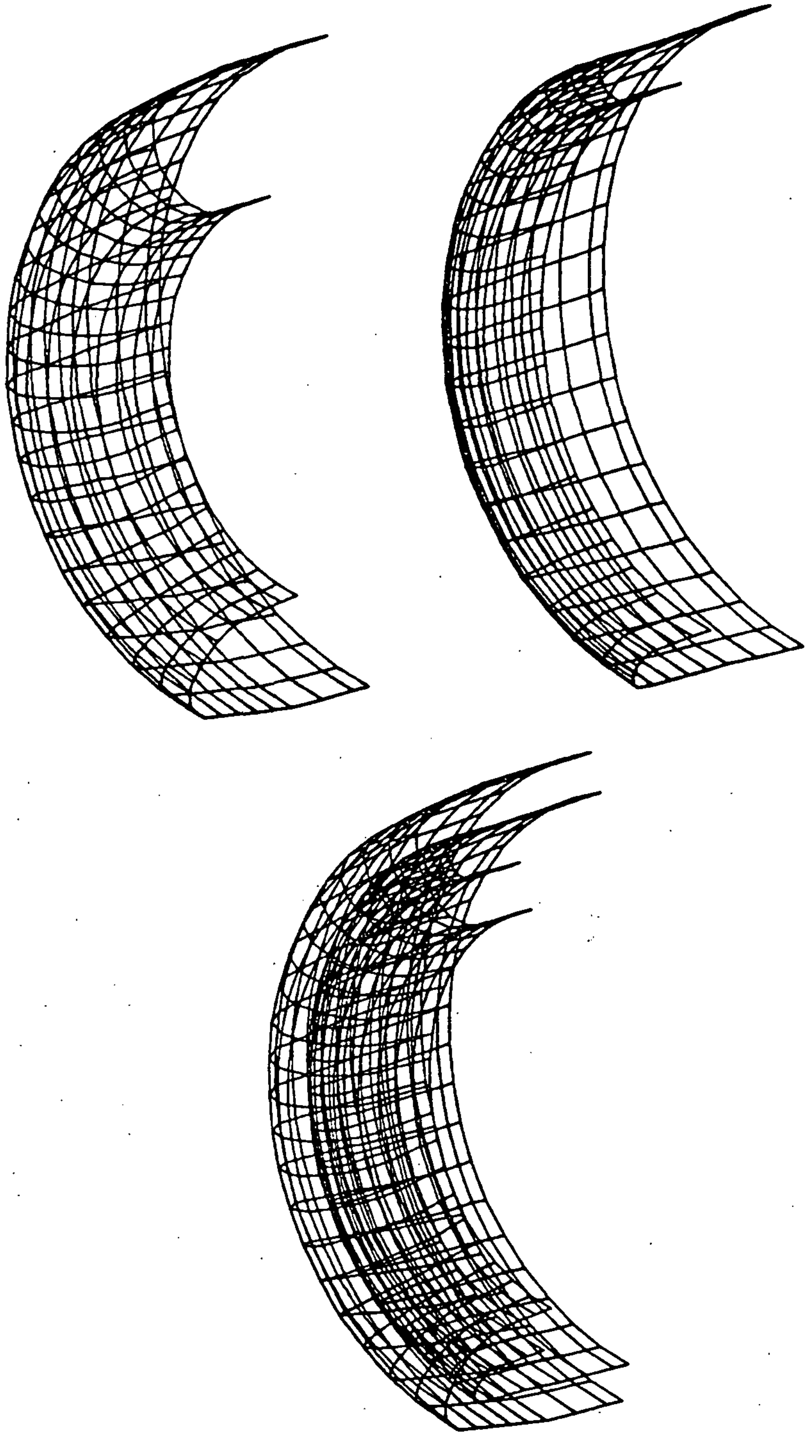

Fig. 2 Cutaway View of Grid Structure for Inner Wall, Outer Wall, and Composite Shape of Turnaround Duct

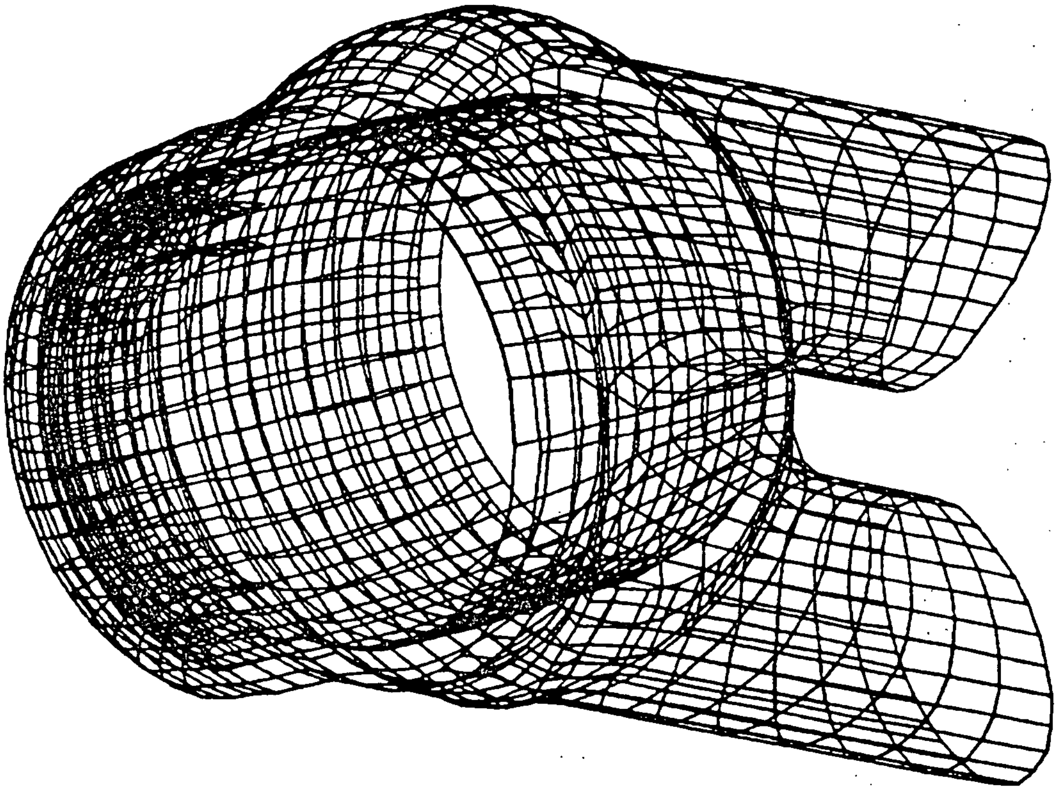

Fig. 3 Sparse Grid Composite of the Computational Model for the HGMII$^+$

2. APPROACH

2.1 GENERAL DESCRIPTION

Computations were performed using the Lockheed-Huntsville Progressive Assembly of Generalized Elements (PAGE) computer code (Ref. 1). PAGE evolved from the previous Lockheed General Interpolants Method (GIM) code (Ref. 2). The new computer code applies to elliptic flow governed by the full Navier-Stokes equations written in three-dimensional conservation law form for a Cartesian coordinate system (Ref. 3). The reader is referred to Ref. 1 and the references cited therein for a detailed description of the PAGE methodology. It will suffice here to state that the code is modular containing geometry, integration, and plotting modules. The computational grid is generated using a versatile algebraic grid generation scheme, and the numerical integration scheme is an explicit predictor-corrector MacCormack type. The integration module is written in CYBER vector FORTRAN and was run on a CYBER 205. The grid generation and plotting were done on scalar machines.

2.1.1 Manifold Grid

Both a low Reynolds number laminar computation and high Reynolds number turbulent computation were performed. Except for incorporation into the model of supporting struts spaced circumferentially at the TAD exit for the turbulent case, the grid structures for both cases were very similar. Minor differences will be discussed in Section 3 of this report. Here we show a course grid structure of the outer and inner walls of the geometry that was generated using the PAGE algebraic grid generator. The inner and outer walls of the bowl and the outside wall of the transfer duct are shown in Fig. 1. Figure 2 contains the inner and outer wall structure of the TAD, and Fig. 3 shows a cutaway view of the composite geometric model. These figures display the full three-dimensional structure of the grid model. Remember, however, that because of the plane of symmetry between the transfer ducts, only half of the geometry was modeled for the numerical integration procedure. Figure 4 shows the orientation of the Cartesian coordinate system used to specify the position of each node in the grid structure.

2.1.2 Analytical

Those characteristics of the computations which were different between the laminar and turbulent calculation will be discussed separately in the next two subsections. Here we present all that is common to both.

The mean flow speed was low enough so that for most of the computational domain the flow could be considered essentially incompressible. For this reason an ideal gas equation of state was not used but instead the slight compressibility of the flow was modeled using the following equation for isothermal flow:

$$\frac{\rho - \rho_o}{\rho_o} = \beta\ (P - P_o) \qquad (1)$$

where ß is an artificial compressibility having a numerical value of 2 x 10^{-6}ft^3/lb, and the zero subscript indicates values at the zeroth iteration. Note that for an ideal gas ß is equal to the recriprocal of the pressure and would thus vary from 1.05 to 1.2x10^{-6}ft^3/lb over the computational domain. At each iteration the time dependent continuity and momentum equations were solved and (1) was used to obtain the static pressure at each node. The total pressure at each node was determined from

$$P_T = P + \rho V^2/2\ . \qquad (2)$$

The solution was thus relaxed to steady state using the asymptotic transient approach.

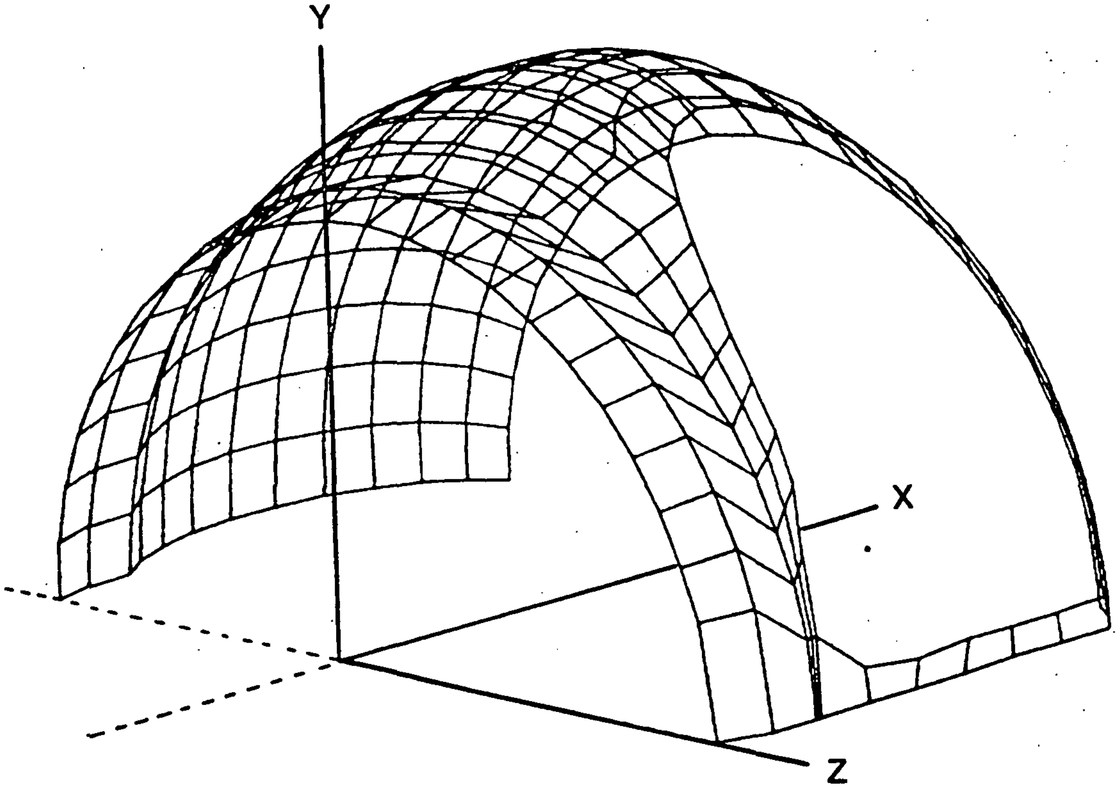

Fig. 4 Cartesian Coordinate System Orientation Used in Computation

Convergence of the solution was based partially on the tendency of the sum of squares of unsteady derivatives of conserved quantities (ρ, ρu, ρv, ρw) to decrease and level off at some minimum value. For both computations these dropped one to two orders of magnitude. In addition, the mass flow rate at selected cross sections was monitored. Specifically the inlet and exit plane as well as an entrance plane to the bowl were selected. Typically these values oscillated with decreasing amplitude to a common steady value.

2.1.3 Initialization

Based on experimental air flow test data measured by Rocketdyne (Ref. 4) for a similar HGM design with two circular transfer ducts the inlet plane to the TAD was initialized with a circumferential variation in pressure and velocity. These are given by

$$P = P'[1 + a + b \sin^2(\theta/2)] \qquad (3)$$

and

$$V = V'(1 + C \cos \theta) \qquad (4)$$

where

$P' = 190.0$ psi
$V' = 380.0$ ft/sec
$a = -0.02$
$b = 0.0441$
$c = 0.04$.

The velocity field through the system was initialized by requiring an appproximate mass balance across planes normal to the mean flow direction. At every point in the computational domain, the density was initially set equal to a value of approximately 1 lbm/ft^3. A total pressure drop between the inlet and exit planes was initialized at five percent for the turbulent cans and 15 percent for the laminar case. The initial average total pressure at the inlet was 206.3 psi for the turbulent case, and 204.1 for the laminar case. The initial average static pressure was 191.4 psi for the turbulent case and 194.4 for the laminar case.

2.2 LAMINAR COMPUTATION

The laminar viscosity used was 10,000 times the laminar value for air under standard conditions. By using this value and a characteristic length equal to the channel width at the inlet, the Reynolds number for the flow was determined as 263.

No slip conditions were enforced at all solid boundaries. The total pressure and flow direction at the inlet plane were held constant. At the exit plane of the transfer duct the static pressure was held constant.

A course mesh computational grid composed of a total of 33,524 nodes was used for the calculations. Figures 5, 6, and 7 show the grid structures for three slices through the system.

2.3 TURBULENT COMPUTATION

With the idea of keeping computational costs within reason, a relatively coarse grid (21059 nodes) was also employed for this calculation (see Figs. 5, 6, and 7). A thin (high Reynolds number) boundary layer profile on the wall was assumed. To this end, free-slip tangency conditions were imposed on the "wall nodes" which were then treated as points near the edge of the boundary layer on the wall. The shear stress on the wall was calculated using (Ref 5)

$$\tau_w = \rho v^{*2} \tag{5}$$

where the friction velocity v^* is obtained from the logarithmic profile expression

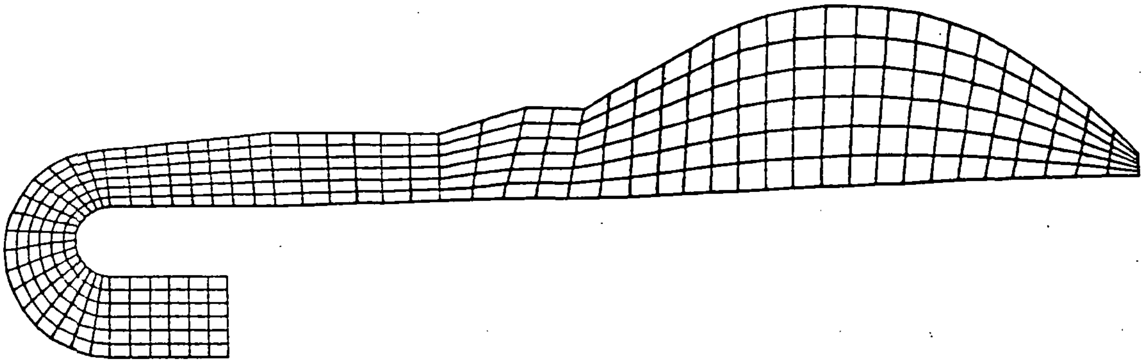

a. Laminar Case

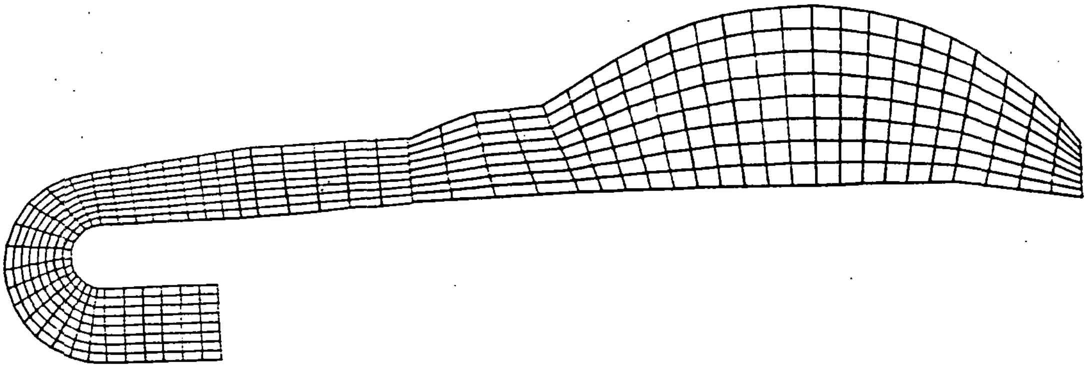

b. Turbulent Case

Fig. 5 Computational Grid in the xy-Plane for TAD and Bowl; (a) Laminar Case, (b) Turbulent Case

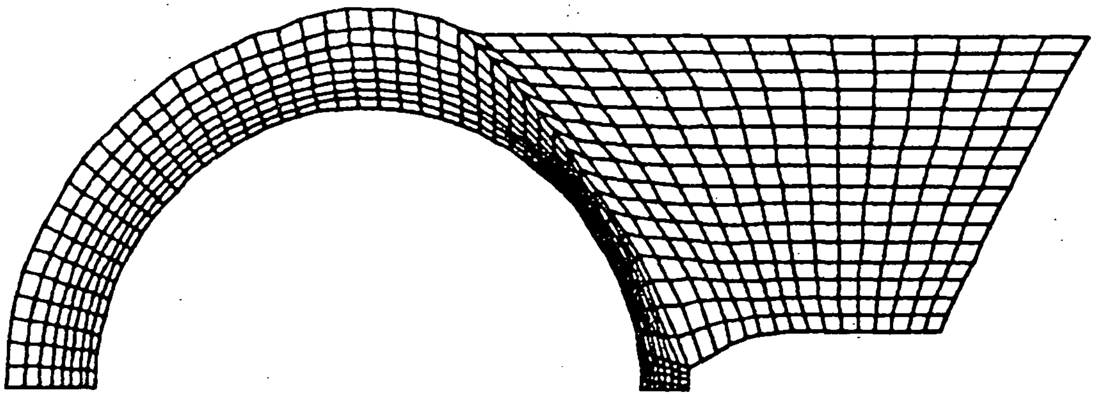

a. Laminar Case

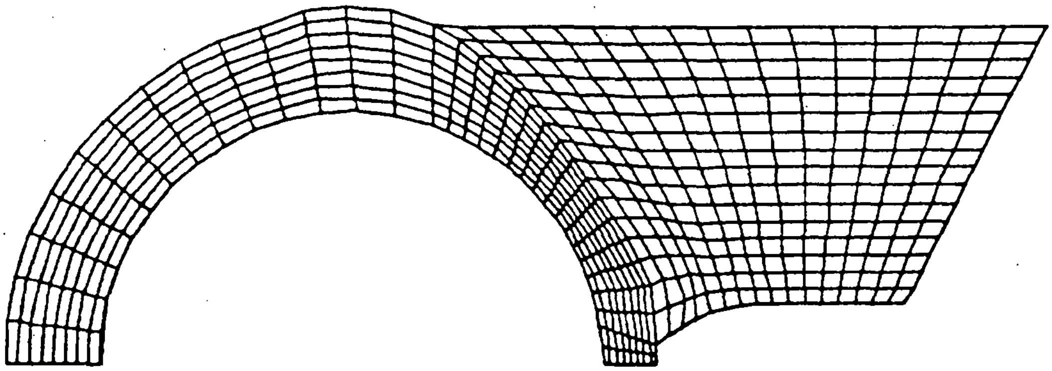

b. Turbulent Case

Fig. 6 Computational Grid for a YZ Slice Through the Bowl and Transfer Duct; (a) Laminar Case, (b) Turbulent Case

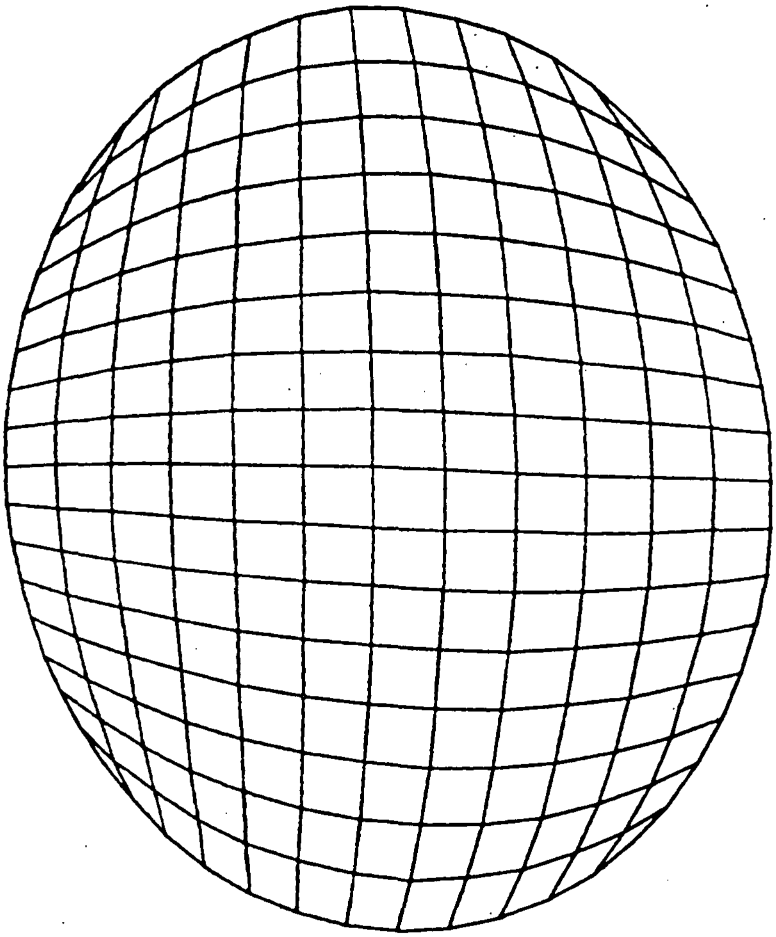

Fig. 7 Computational Grid for a Cross Section of the Transfer Duct Midway into the Duct

$$\frac{u}{v^*} = \frac{1}{k} \ln (E \rho v^* y/\mu) \tag{6}$$

by a simple Newton-Raphson iteration procedure. Here u is the magnitude of the velocity on the first point off the wall, k and E have numerical values of 0.4 and 9.0, respectively, y is the distance to the first point off the wall, and μ is the laminar viscosity for air. The velocity for the point "on the wall" is determined from the shear stress/velocity gradient relation (corrected for tangency) given by

$$u_t = u - y \tau_w/(\mu + \mu_t) \tag{7}$$

The turbulent viscosity μ_t is obtained using a Prandtl-Van Driest mixing length model where

$$\mu_t = \rho \ell^2 \omega \tag{8}$$

and ℓ is given by (Ref 6)

$$\frac{\ell}{H} = 0.14 - 0.08 (1 - \frac{y}{H})^2 - 0.06 (1 - \frac{y}{H})^4 . \tag{9}$$

H is a hydraulic radius determined for each part of the geometry, and ω is the magnitude of the vorticity.

The magnitude of the laminar viscosity used was 1.245×10^{-5} lbm/ft-sec. This yields a Reynolds number of 2.5×10^6 using the average speed at the TAD inlet and the width of the TAD inlet. The turbulence eddy viscosity ranged in magnitude from 0.0004 near the walls to 0.30 lbm/ft-sec at mid channel in regions of high vorticity. For these computations the total pressure and velocity direction were held fixed at the inflow boundary and the static pressure was held fixed at the outflow boundary.

3. RESULTS

3.1 LAMINAR COMPUTATION

This high viscosity low Reynolds number calculation was performed not so much as a means of providing comparison with experimental data but for the comparison with other similar computations in the same geometry performed with different computer codes. For this reason comparison of pressure lasser to experimental results will not be made. We will show flow fields and pressure distributions obtained for cross sections through each part of the geometry.

Figures 8, 9, and 10 shows the velocity vectors, velocity constant, and static pressure contours for a slice through the TAD-bowl corresponding to the xy-plane. Note that all composite plots of TAD and bowl were made from two separate plots drawn to the same scale. Photographic reduction was necessary of the TAD section to form the composite. Thus, vectors, numbers and line widths appear smaller in the TAD section of the composite. The velocity profile display typical parabolic shape. Even though the density of vectors in the turn is high, careful observation will show that the maximum speed shifts from mid channel before the turn to a position closer to the inner wall in the turn. This is more evident in Fig. 9. At the beginning of the turn the velocity is lower at the outer wall and after the turn it is lower at the inner wall. Downstream of the turn again the velocity maintains a laminar channel profile. The pressure contours downstream of the turn, in Fig. 10, show typical channel flow structure. In the turn, except for the contour nearest the inner wall corresponding to the lowest pressure, the contours begin on the inner wall and bend downstream to terminate on the outer wall. The curvature of the profiles in the turn is a

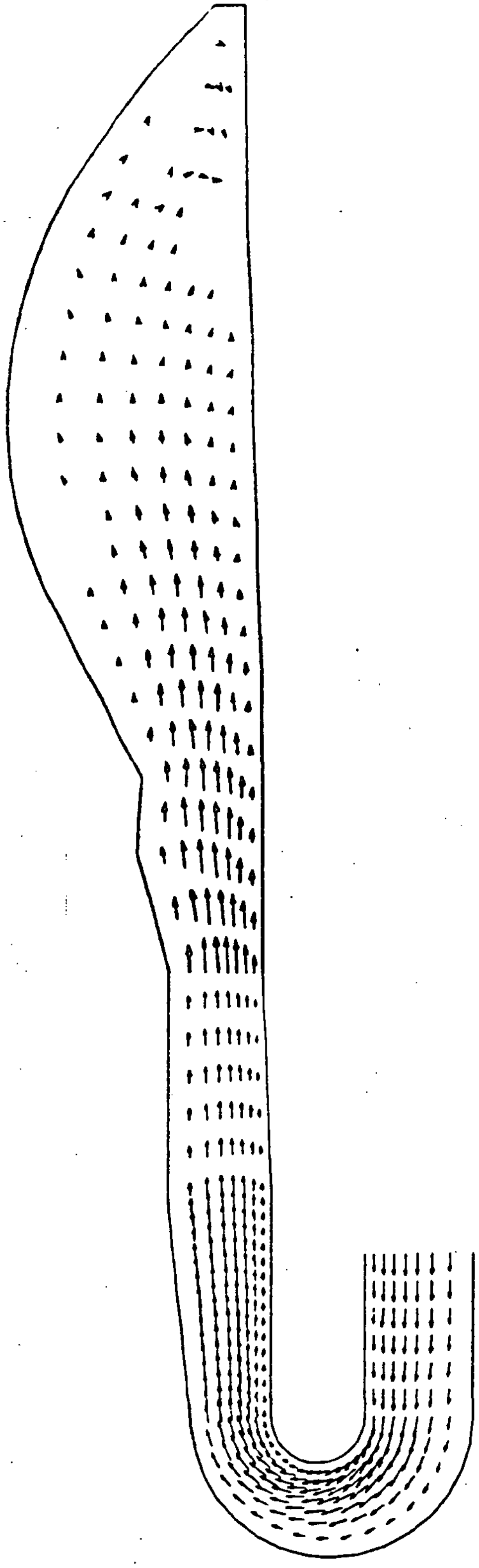

Fig. 8 Velocity Vectors (Laminar Case) for a TAD-Bowl Cross Section Corresponding to the xy-Plane

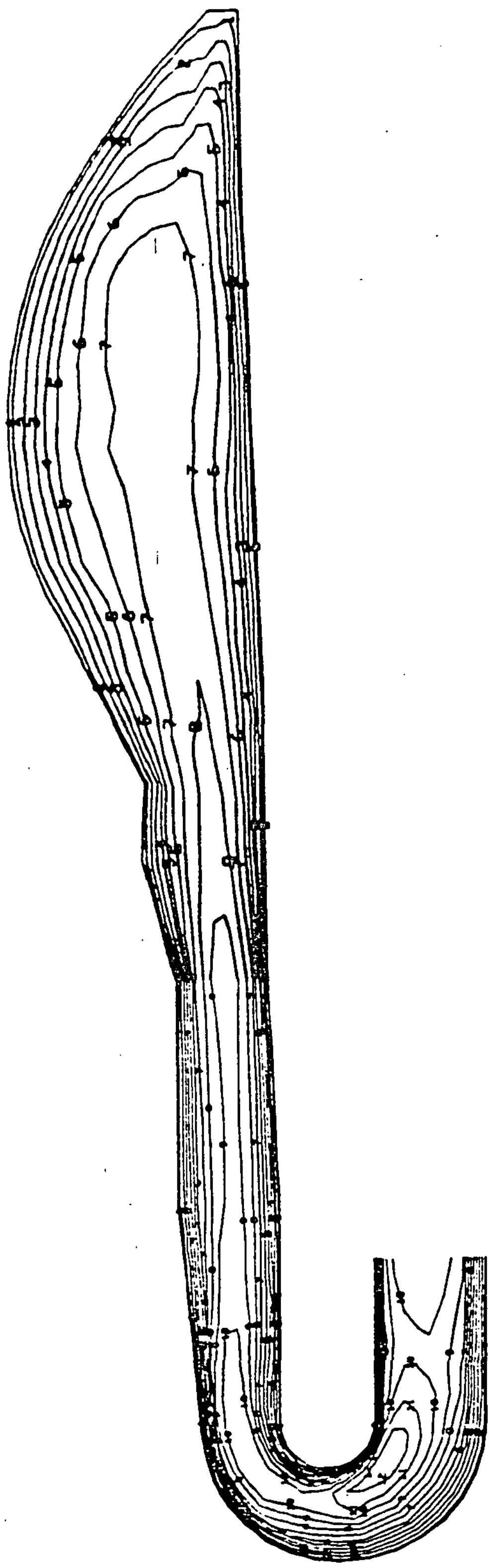

Fig. 9 Velocity Contours (Laminar Case) for a TAD-Bowl Cross Section Corresponding to the xy-Plane (Maximum Velocity is 348 ft/sec)

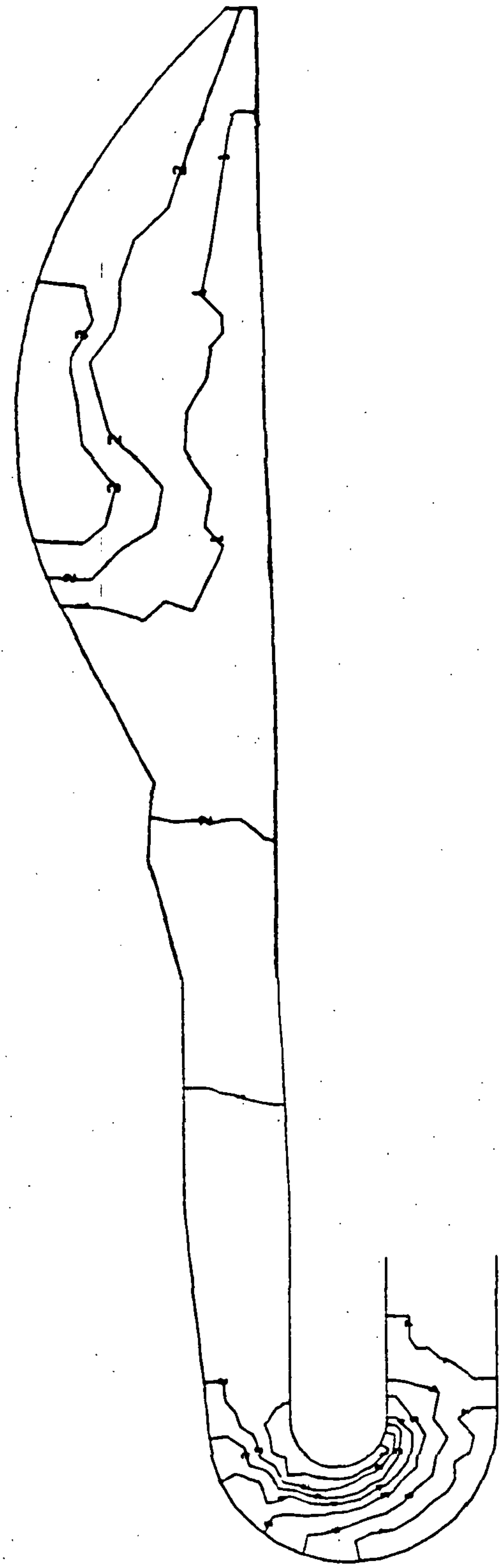

Fig. 10 Static Pressure Contours for a TAD-Bowl Cross Section Corresponding to the xy-Plane (Pressure Range is 178.5 - 197.0 psi)

function of the viscosity: the lower the viscosity the more curvature. Because of the coarseness of the grid, the profiles are jagged rather than smooth curves. The pressure ranges from 196.5 psi at the TAD inlet to 181.9 psi at its exit, and from 179.2 psi near the outer wall of the bowl to 177.8 near the bowl inner wall. Contour scales in TAD and bowl are different.

Figure 11 presents similar results for a central yz-slice through the bowl and transfer duct. As the flow enters the transfer duct at the top of the figure its velocity is considerably larger than at the bottom. At a central cross section of the transfer duct the maximum speed has moved essentially to mid channel. We will denote circumferential locations in the bowl relative to the central position between the two transfer ducts. In Fig. 4 this corresponds to the z-axis. Using this convention, notice that the velocity vector plot in Fig. 11 indicates a stagnation region at approximately 23 deg. The pressure and velocity contours in that same figure corroborate the previous discussion of the velocity field. The pressure range is from 172.9 to 180.2 psi.

Velocity vectors, velocity profiles, and static pressure contours in a cross section midway down the transfer duct is shown in Fig. 12. In the vector plot a secondary flow double swirl pattern can clearly be seen. The view is looking down the transfer duct toward the bowl. A primary swirl to the right and occupying about two-thirds of the duct is clockwise, and a second counterclockwise swirl is evident to the left. The velocity contours show that the largest axial velocities are very near the upper right quadrant of the duct. The pressure gradient across the duct at this position is very slight, the range being only 1.3 psi.

Of particular interest is the determination of the total pressure loss through the system. One procedure for calculating this is to average the total pressure over planes normal to the mean flow direction from inflow plane to outflow plane and display the results as a graph of average pressure

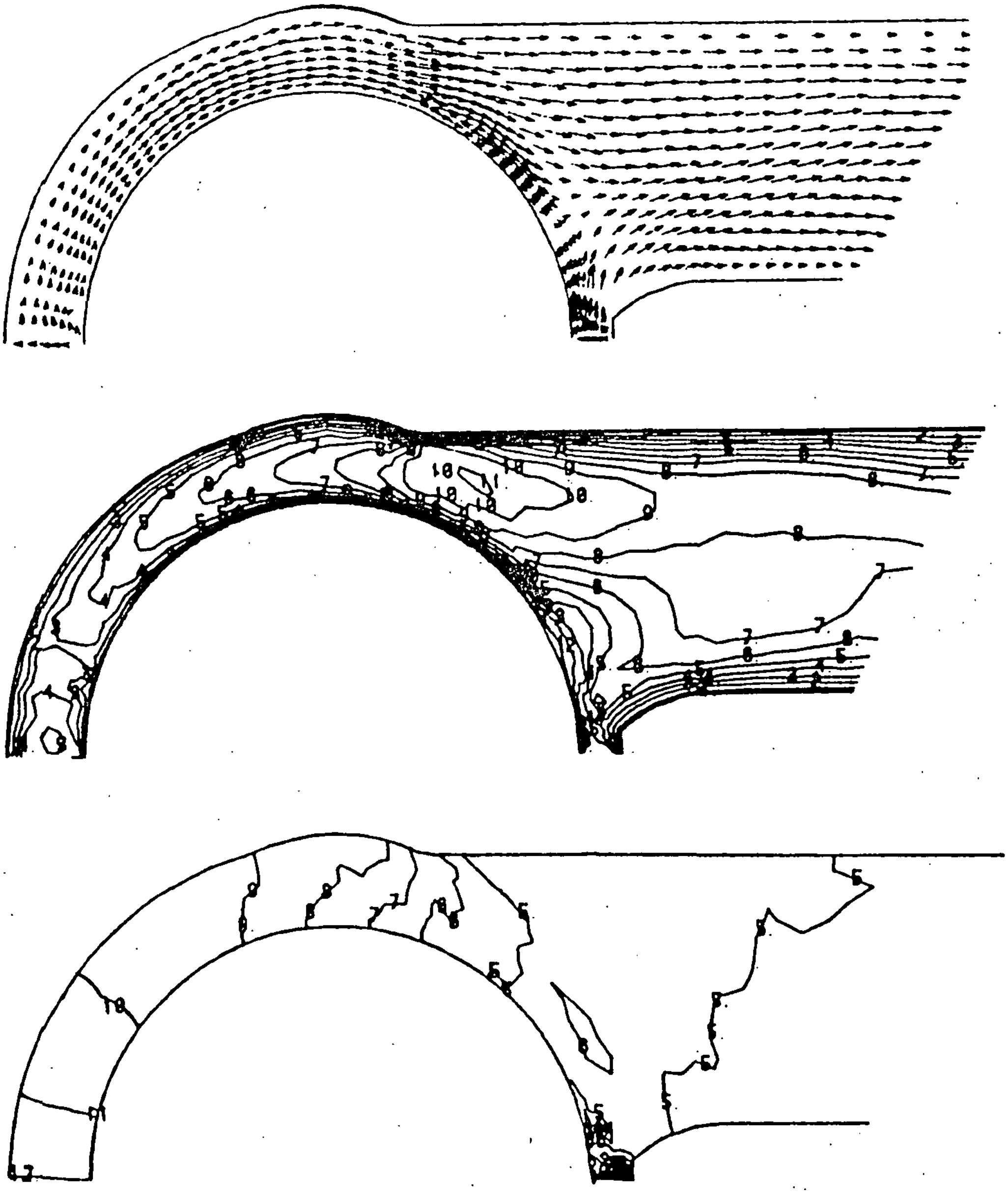

Fig. 11 Velocity Vectors, Velocity Contours, and Static Pressure Contours (Laminar Case) for a yz Cross Section Corresponding to the Center Plane of the Transfer Duct (Maximum Velocities 294 ft/sec, and Pressure Range is 171.5 - 187.8 psi)

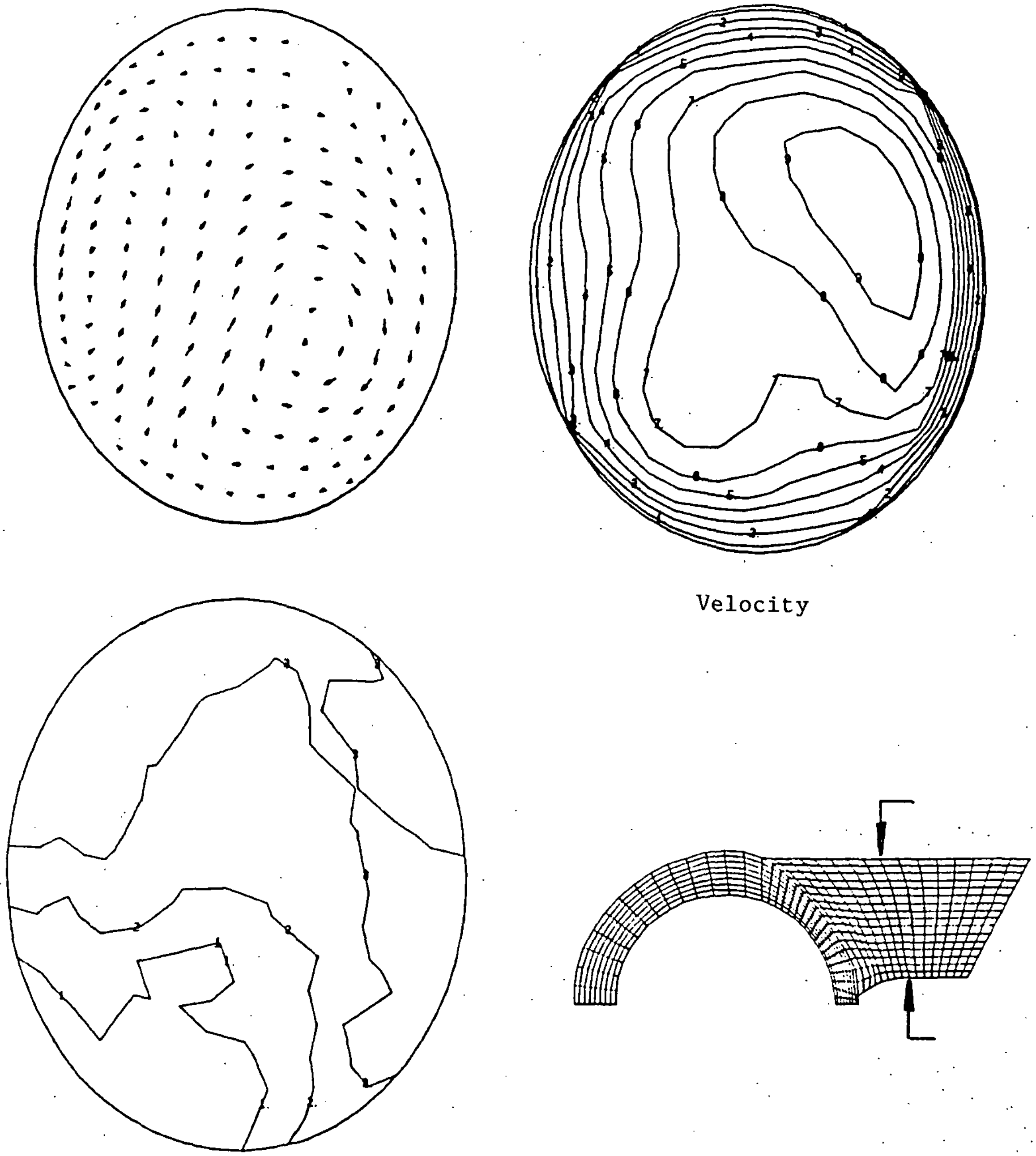

Velocity

Pressure

Fig. 12 Velocity Vectors, Velocity Contours, and Static Pressure Contours (Laminar Case) Corresponding to a Central Cross Section of the Transfer Duct (Maximum Velocity is 238 ft/sec, and Pressure Difference is 1.3 psi) versus distance along a centerline through the manifold. We calculate a mass averaged total pressure. A method to do this is to integrate over the j-th plane using the equation

$$\overline{P_{T,j}} = \frac{\int_j P_T d\dot{m}}{\int_j d\dot{m}} \qquad (10)$$

where

$$d\dot{m} = \rho\vec{V} \cdot d\vec{A}.$$

Since however the space is discretized the integrals must be changed to summations. For our calculations we used

$$\overline{P_{T,j}} = \frac{\sum_i \bar{P}_{T,i} \, \overline{(\rho_i \vec{V})_i} \cdot d\vec{A}_i}{\sum_i \overline{(\rho_i \vec{V}_i)_i} \cdot d\vec{A}} \qquad (11)$$

where the summation is over all quadrilateral elements which make plane j, and the bar under the summation indicates average values over the i-th element. Results for the laminar case are plotted in Fig. 13. Sections of the geometry and pressure losses in each section are indicated in the figure. The discontinuity in the graph occurs because cross-sections are translated from the bowl to the transfer duct when the bowl cross-section coincides with the center of the duct. Clearly, the largest percentage of the pressure loss occurs in the turnaround duct.

3.2 TURBULENT COMPUTATION

As a means of testing the effectiveness of the turbulence model discussed previously for application to a course grid computational domain, an axisymmetric calculation was performed on a 270-node turnaround duct geometry. After ten thousand iterations using an average time step of 0.5-microseconds the solution was judged to be converged. Velocity vectors,

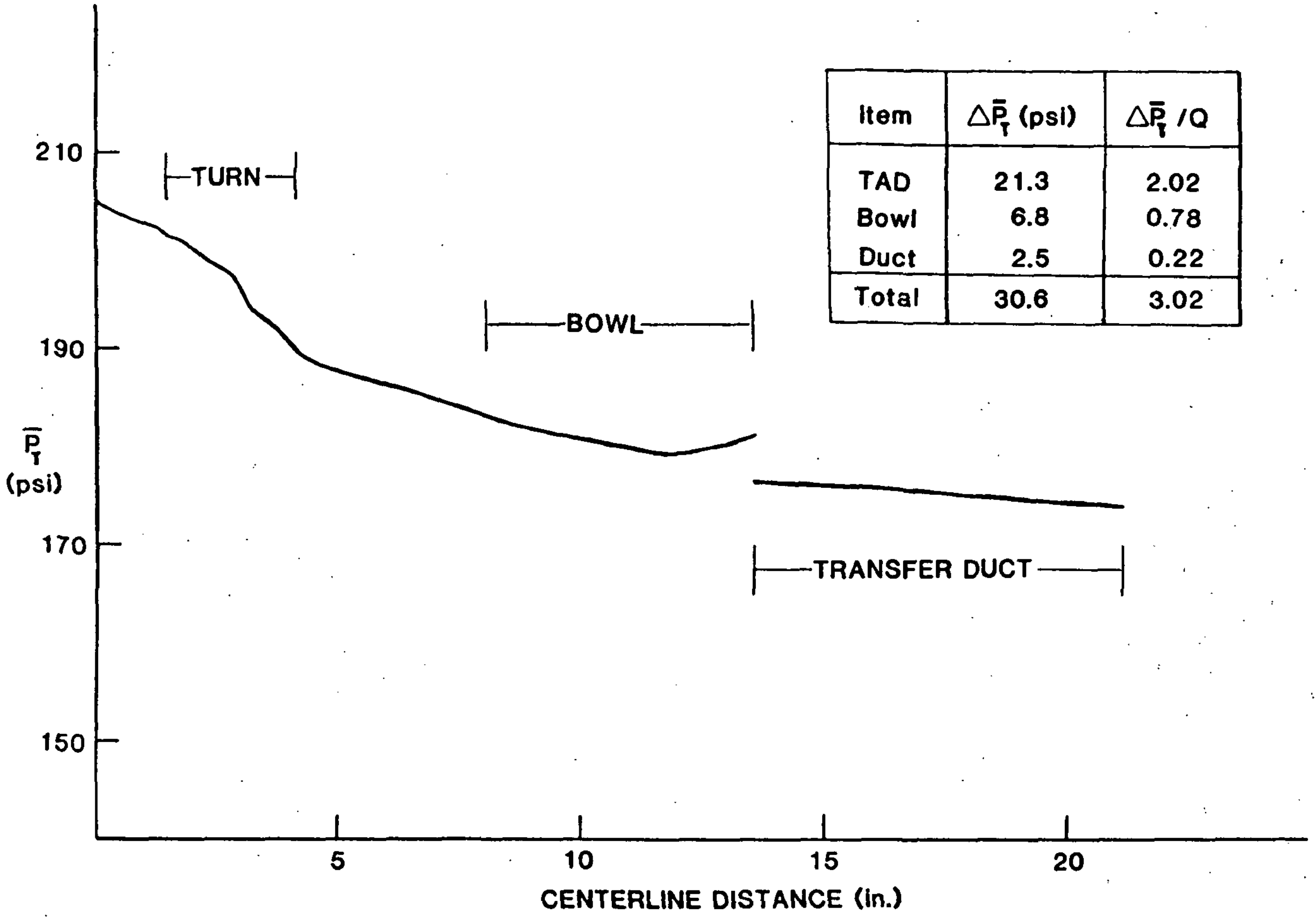

Item	$\Delta\bar{P}_T$ (psi)	$\Delta\bar{P}_T$ /Q
TAD	21.3	2.02
Bowl	6.8	0.78
Duct	2.5	0.22
Total	30.6	3.02

Fig. 13 Mass-Averaged Total Pressure Distribution Through the Manifold (Laminar Case). Definition of P_T Given in Eq (11).

velocity contours, and static pressure contours are shown in Fig. 14. The typical turbulent profile of the velocity vectors is in contrast to those in the laminar case. The shift in maximum speed from the inner wall at the beginning of the turn to the outer wall at the turn exit can clearly be observed in both the vector and contour plots. Also note that the influence of the turn is clearly indicated upstream of the turn by a distance of at least one turn radius. The pressure contours are in striking contrast to those for the high viscosity laminar case. Near the inner or outer wall the contours have maximum curvature, beginning and ending on the same wall. The total pressure distribution is displayed in Fig. 15. Here the pressure coefficient C_p is plotted as a function of distance along the center line. C_p is defined as

$$C_p = \frac{P_T - P_{To}}{Q_o} \tag{12}$$

where P_{To} and Q_o are the average total pressure and dynamic pressure at the inlet plane, respectively. The total C_p was 0.32.

For the turbulent manifold computation a model of supporting struts between the inner and outer wall at the exit of the TAD was incorporated into the course grid structure. Without major modifications to the grid the actual shape of the six struts and six spacers of two different widths (from 0 to 180 deg) could not be modeled. It was thus decided to make an approximate model of the presence of the struts with five rectangular structures creating, to within one percent, the same blocked area as the struts and spacers in the actual geometry. The grid structure of the strut region is shown in Figs. 16 and 17. Clearly the grid is not dense enough to resolve fine details of the flow around the struts.

Figures 18, 19, and 20 present velocity vectors, velocity contours, and pressure contours, respectively, for an xy cross section through the TAD and bowl corresponding to a circumferential position of 90 deg. Note again that since all composite plots showing a cross section of the TAD and bowl were

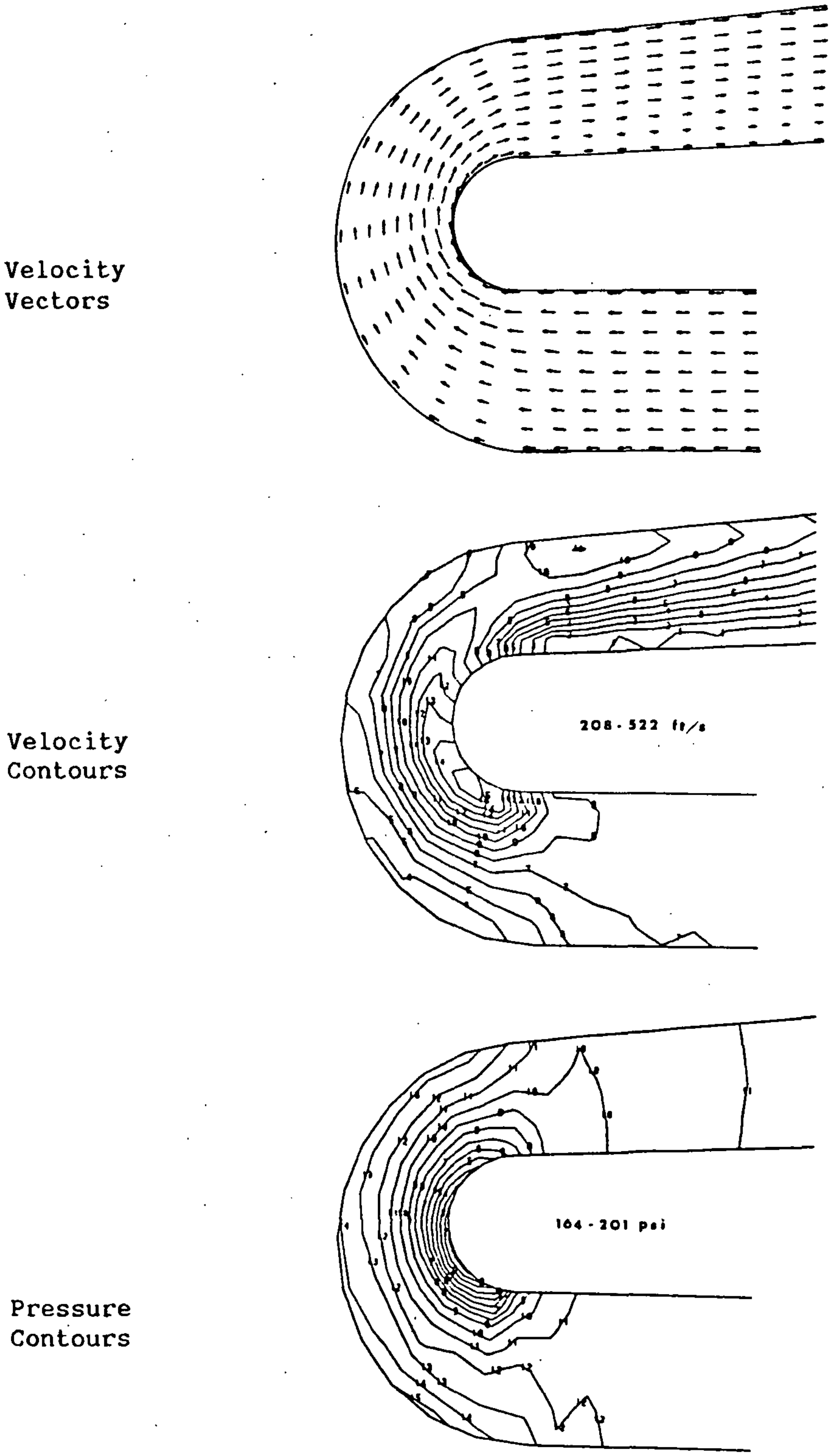

Velocity Vectors

Velocity Contours

Pressure Contours

Fig. 14 Velocity Vectors (Top), Velocity Contours, and Static Pressure Contours (Bottom) for the 270 Node Axisymmetric TAD Turbulent Case

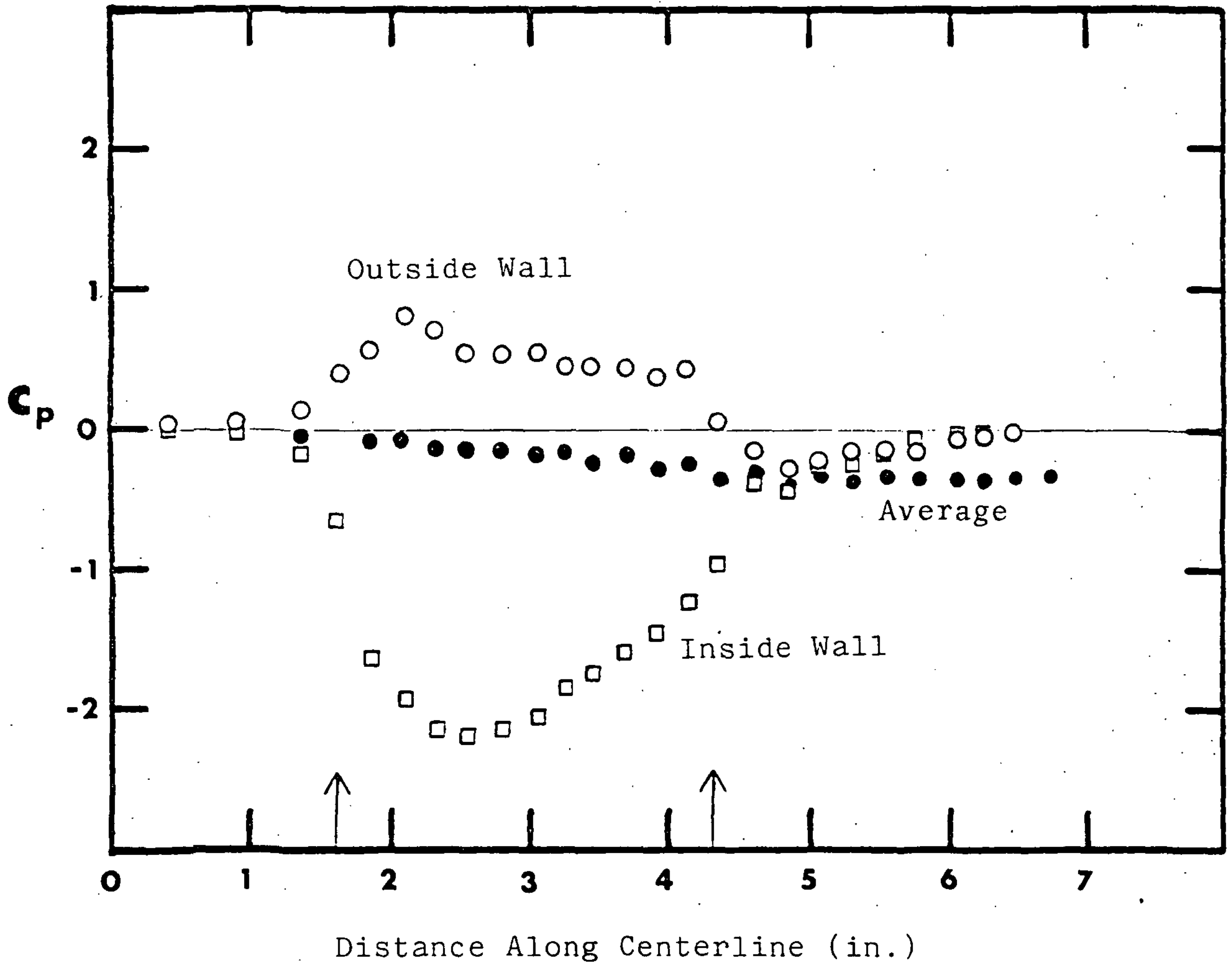

Fig. 15 Total Pressure Coefficient for the Axisymmetric TAD Turbulent Computation (Net C_p is 0.32)

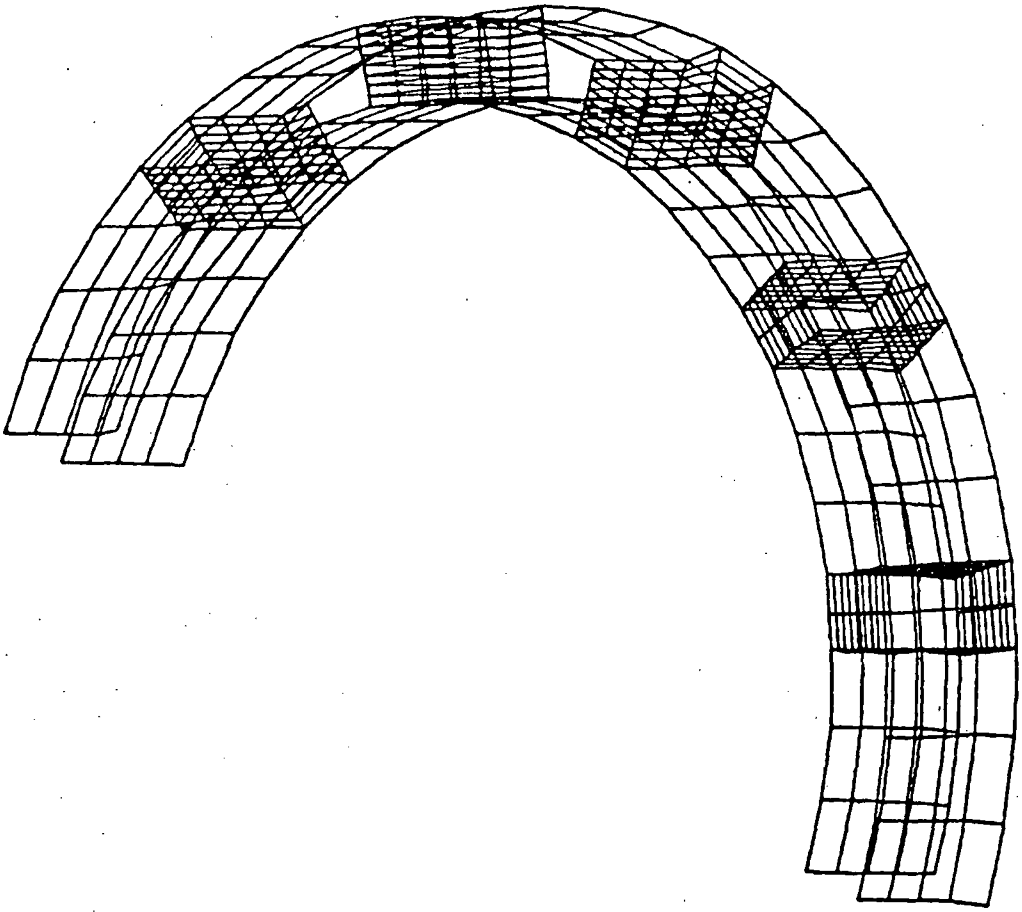

Fig. 16 Partial Grid Structure of Inner and Outer Walls of Manifold Model at the TAD-Bowl Intersection Showing Shape and Orientation of Grid Model for Struts

ORIGINAL PAGE IS
OF POOR QUALITY

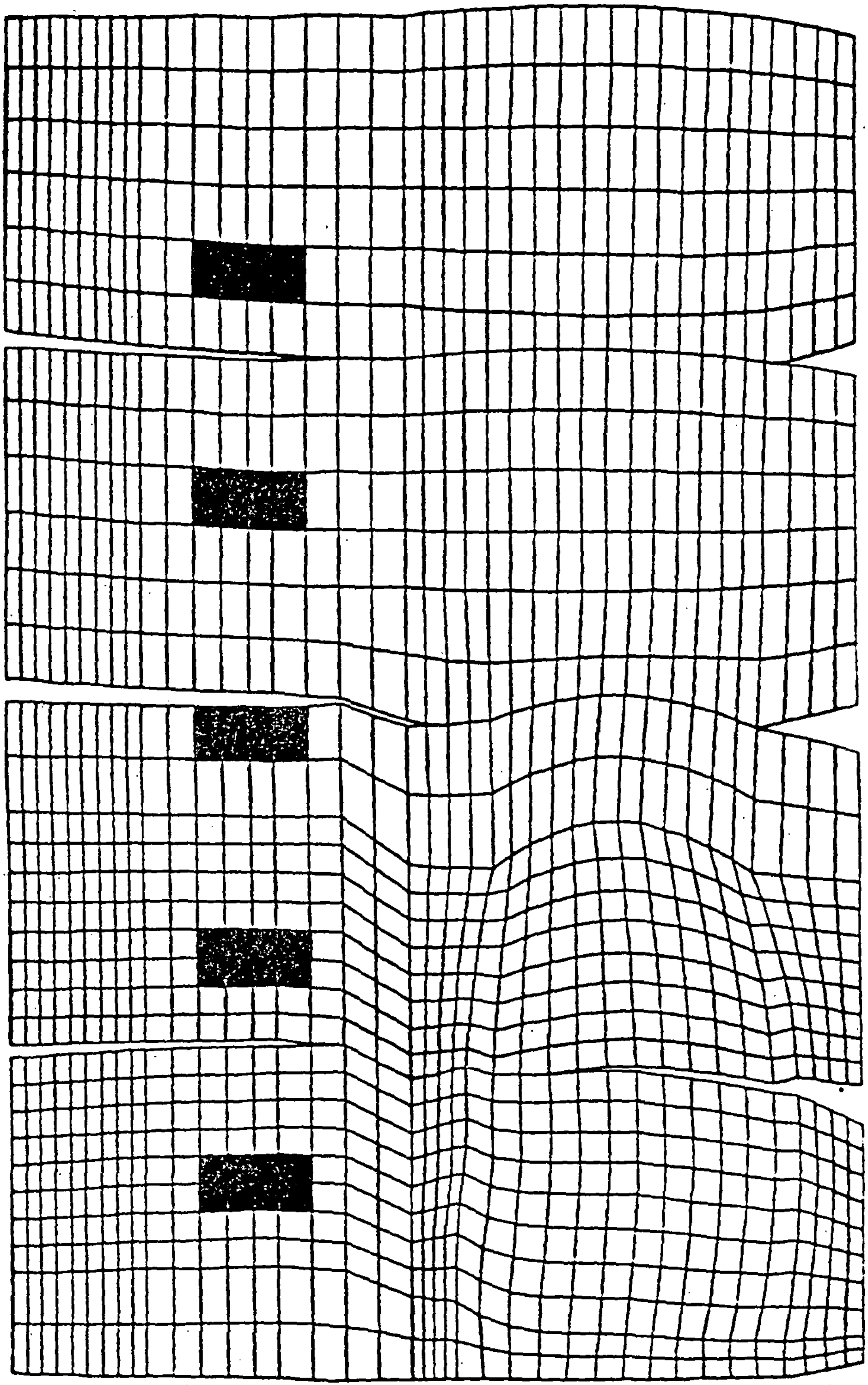

Fig. 17 Unwrapped Mid-Plane Grid Structure of TAD-Bowl from End of Turn to Back of Bowl (Shaded Areas Indicate Positions of Struts)

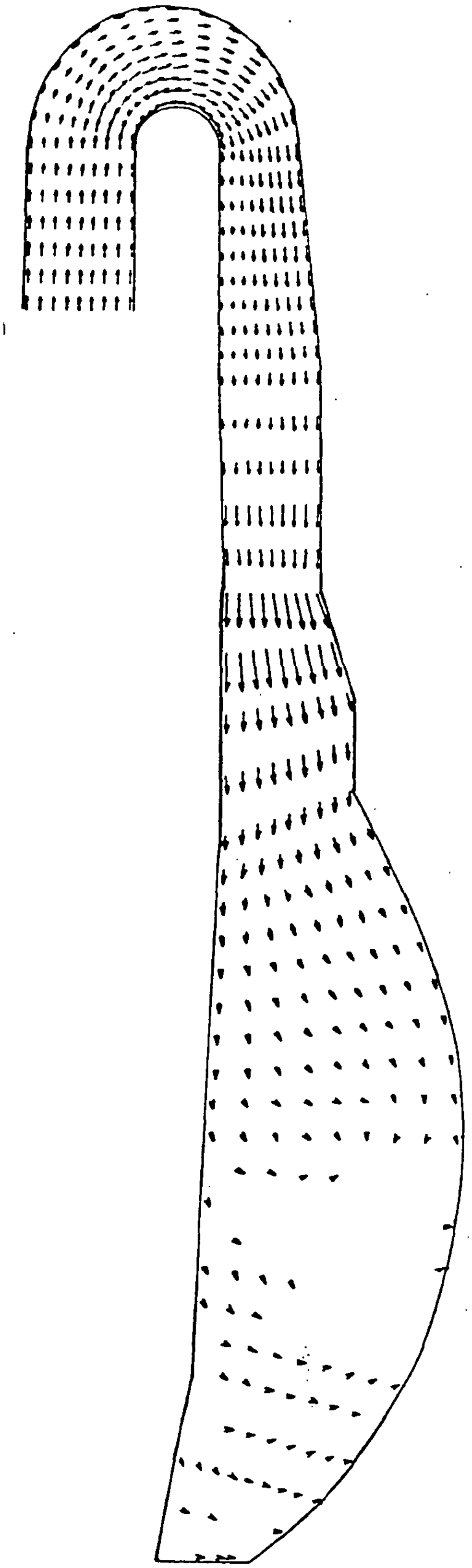

Fig. 18 Velocity Vectors in the Cross-Sectional Plane of TAD and Bowl Corresponding to a Circumferential Position of 90-deg

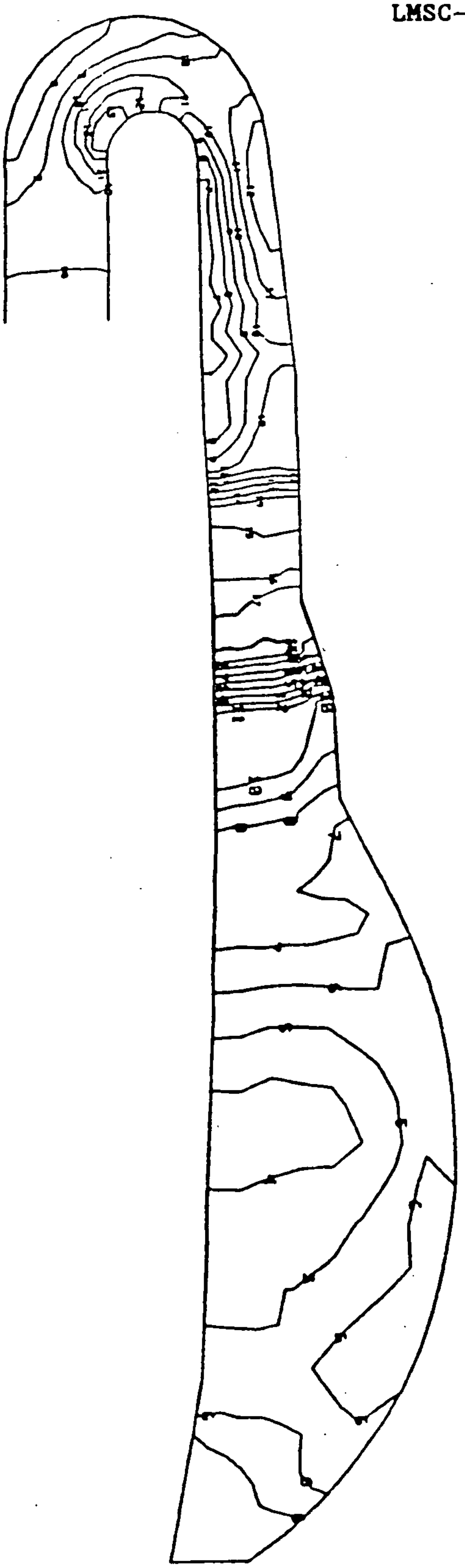

Fig. 19 Velocity Contours in the Cross-Sectional Plane of TAD and Bowl Corresponding to a Circumferential Position of 90-deg (Velocity Range is 19.2 - 595 ft/sec)

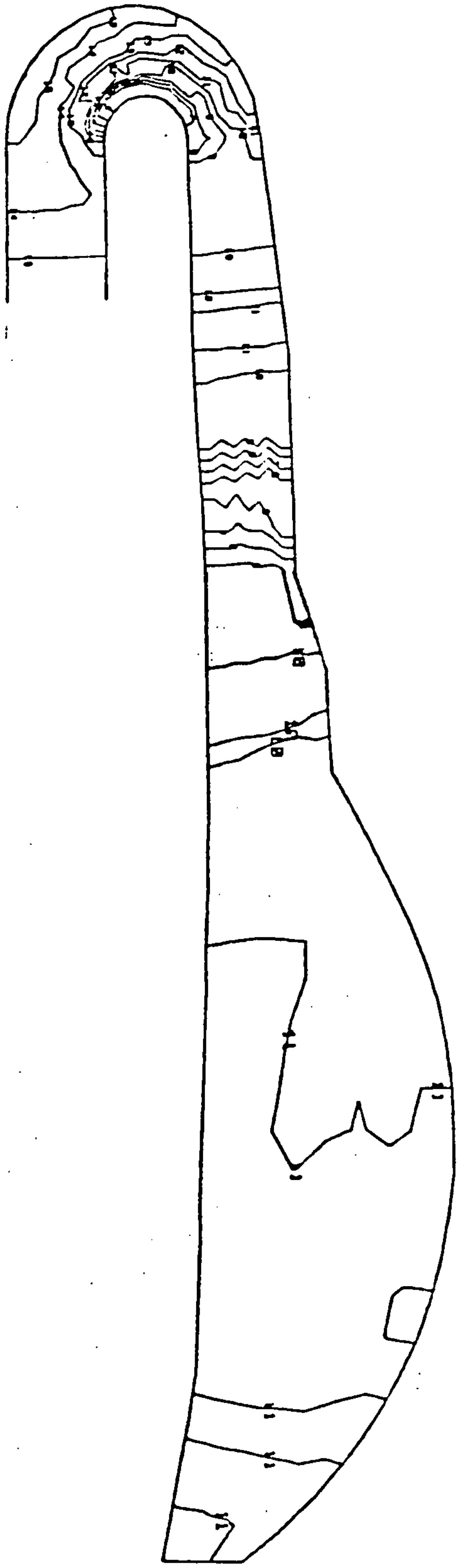

Fig. 20 Static Pressure Contours in the Cross-Sectional Plane of TAD and Bowl Corresponding to a Circumferential Position of 90-deg (Pressure Range is 160.6 - 192.6 psi)

constructed of two separate plots drawn to the same scale, photographic reduction of the TAD section causes vectors, numbers, and linewidths to appear smaller in that section. In all these figures the behavior before, during, and after the turn is almost identical to that seen previously for the axisymmetric TAD.

Again no separation resulted downstream of the turn. The influence of the struts in accelerating the fluid through that region can be clearly seen in each figure. Similar results for circumferential locations of 180 deg (side opposite the transfer ducts) and 0 deg (in between the transfer ducts) can be seen in Figs. 21 through 26.

Velocity vectors, velocity contours, and static pressure contours for a central yz-plane in the bowl-transfer duct are presented in Fig. 27. The flow velocity is seen to increase circumferentially from 180 deg reaching a maximum at the right hand side of the transfer duct. Note that the perspective in Fig. 27 is viewed from the top of the right transfer duct of the manifold. In this same direction along the inside wall the static pressure decreases and reaches a maximum at approximately 25 deg. Just below this position the flow vectors and the velocity contours indicate a stagnation region.

Additional details of the flow characteristics in the right transfer duct are shown in Figs. 28 through 32. Velocity vectors in the diagonal views displayed in Figs. 30 and 31 indicate a low velocity region on the lower left side of the transfer duct in which recirculation could occur. Results in a midcross-section of the right transfer duct as viewed from the main injector into the bowl are given in Fig. 32. The velocity vectors clearly show a secondary flow swirl with counterclockwise rotation. Figure 33 presents flow visualization results obtained in a similar geometry by investigators at NASA-MSFC in a water flow test (Ref 7). The observed swirl direction and the region of recirculation provide qualitative agreement with the numerical results just presented.

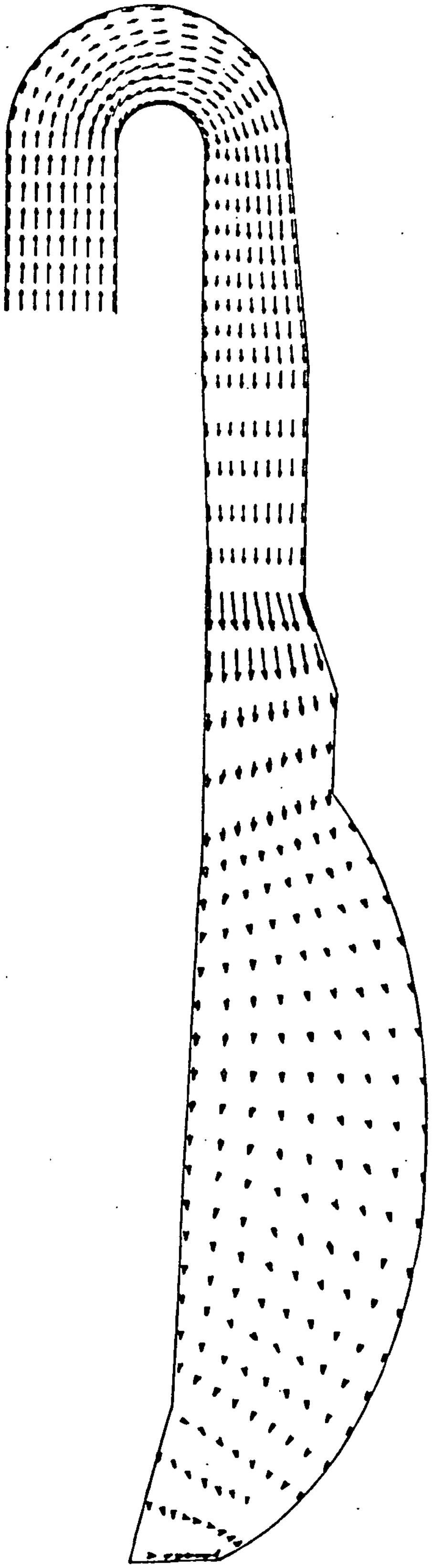

Fig. 21 Velocity Vectors in the Cross-Sectional Plane of TAD and Bowl Corresponding to a Circumferential Position of 180-deg

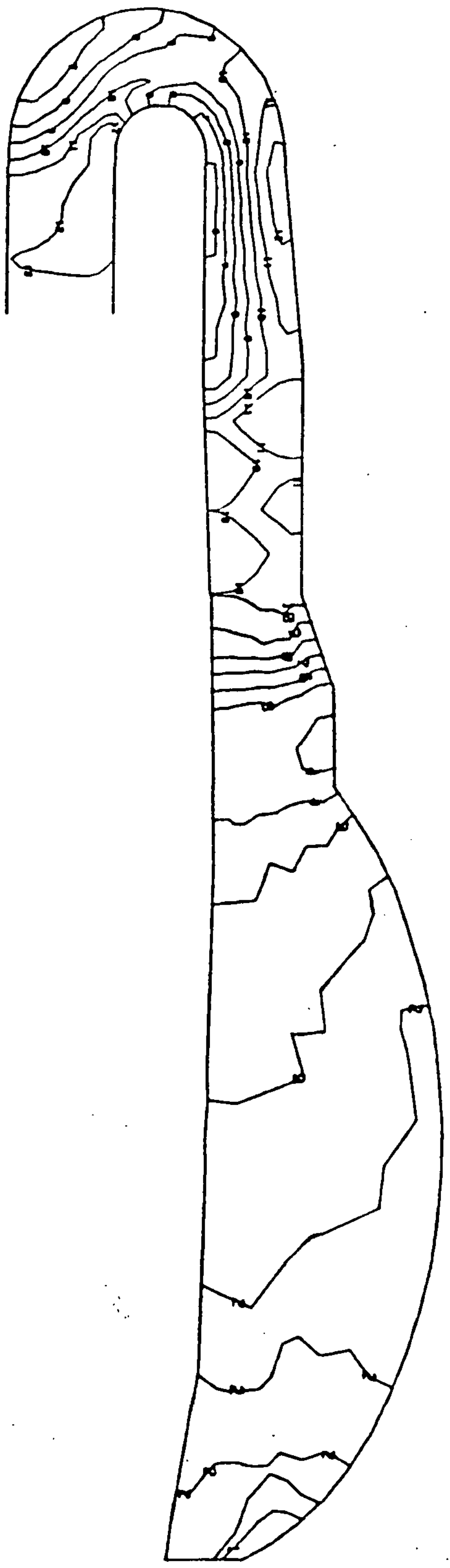

Fig. 22 Velocity Vectors in the Cross-Sectional Plane of TAD and Bowl Corresponding to a Circumferential Position of 180-deg (Velocity Range is 19.2 - 441.5 ft/sec)

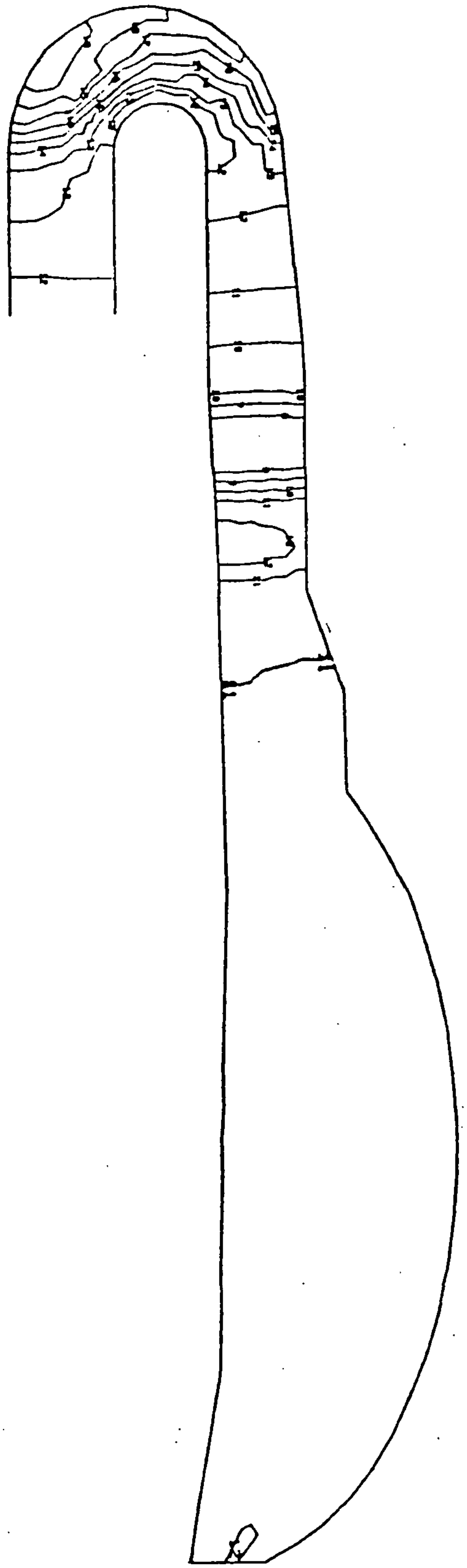

Fig. 23 Static Pressure Contours in the Cross-Sectional Plane of TAD and Bowl Corresponding to a Circumferential Position of 180-deg (Pressure Range is 174.8 - 210.3 psi)

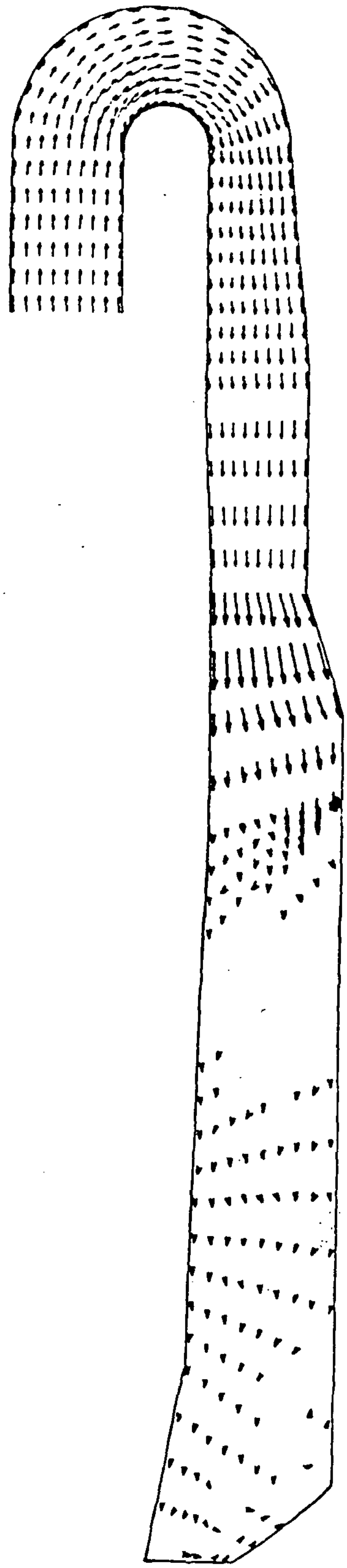

Fig. 24 Velocity Vectors in the Cross-Sectional Plane of TAD and Bowl Corresponding to a Circumferential Position of 0-deg

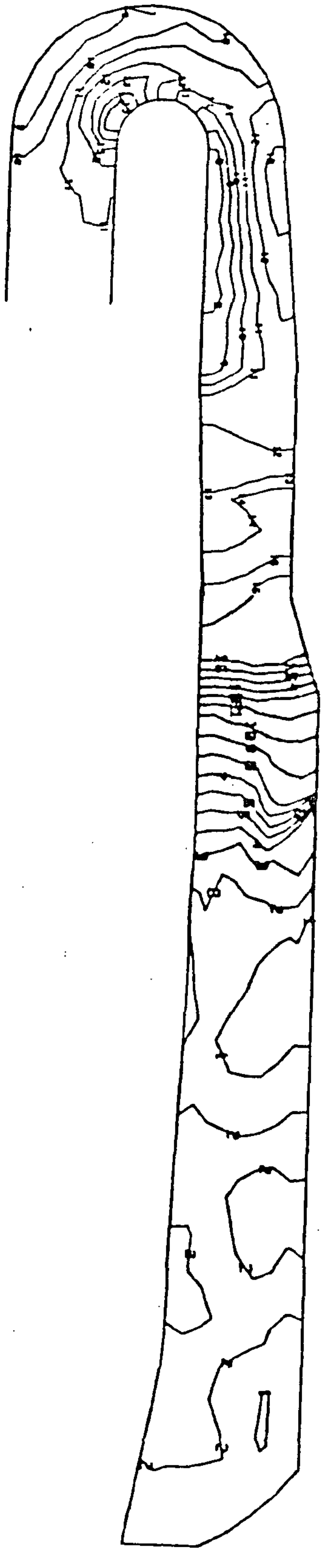

Fig. 25 Velocity Contours in the Cross-Sectional Plane of TAD and Bowl Corresponding to a Circumferential Position of 0-deg (Velocity Range is 134.4 - 590.0 ft/sec)

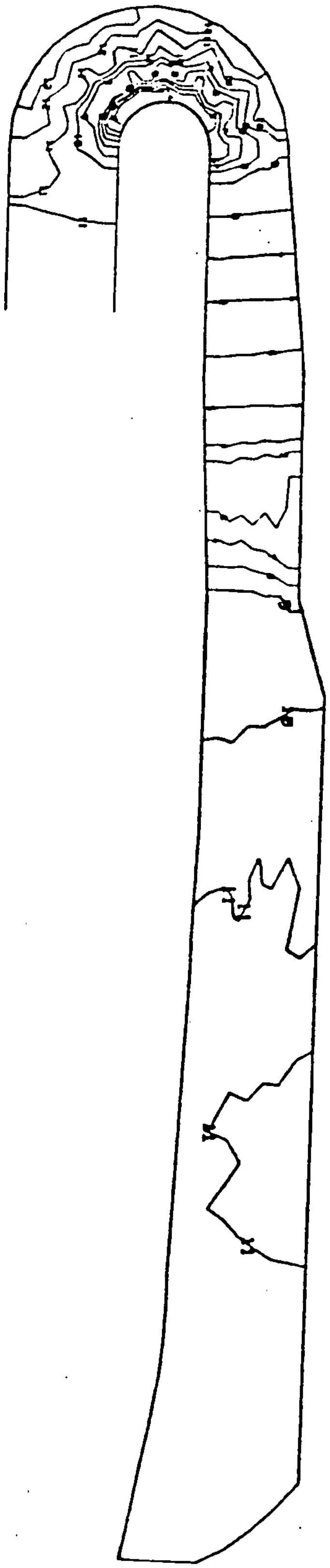

Fig. 26 Static Pressure Contours in the Cross-Sectional Plane of TAD and Bowl Corresponding to a Circumferential Position of 0-deg (Pressure Range is 167.7 - 199.7 psi)

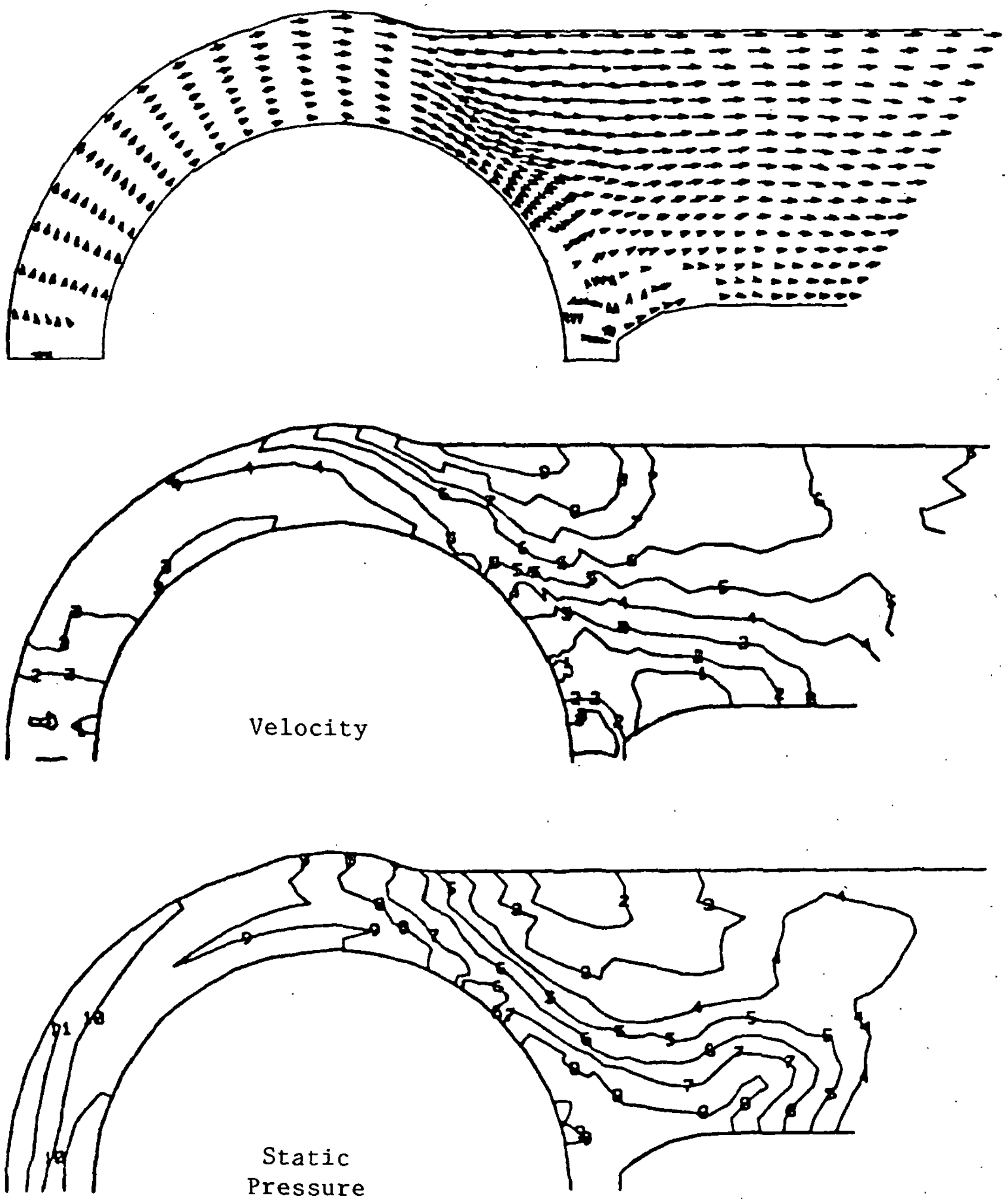

Fig. 27 Velocity Vectors, Velocity Contours, and Static Pressure Contours (Bottom) for a yz-Plane in the Bowl and Transfer Duct (Velocity Range is 40 - 360 ft/sec and Pressure Range is 180 - 187.5 psi)

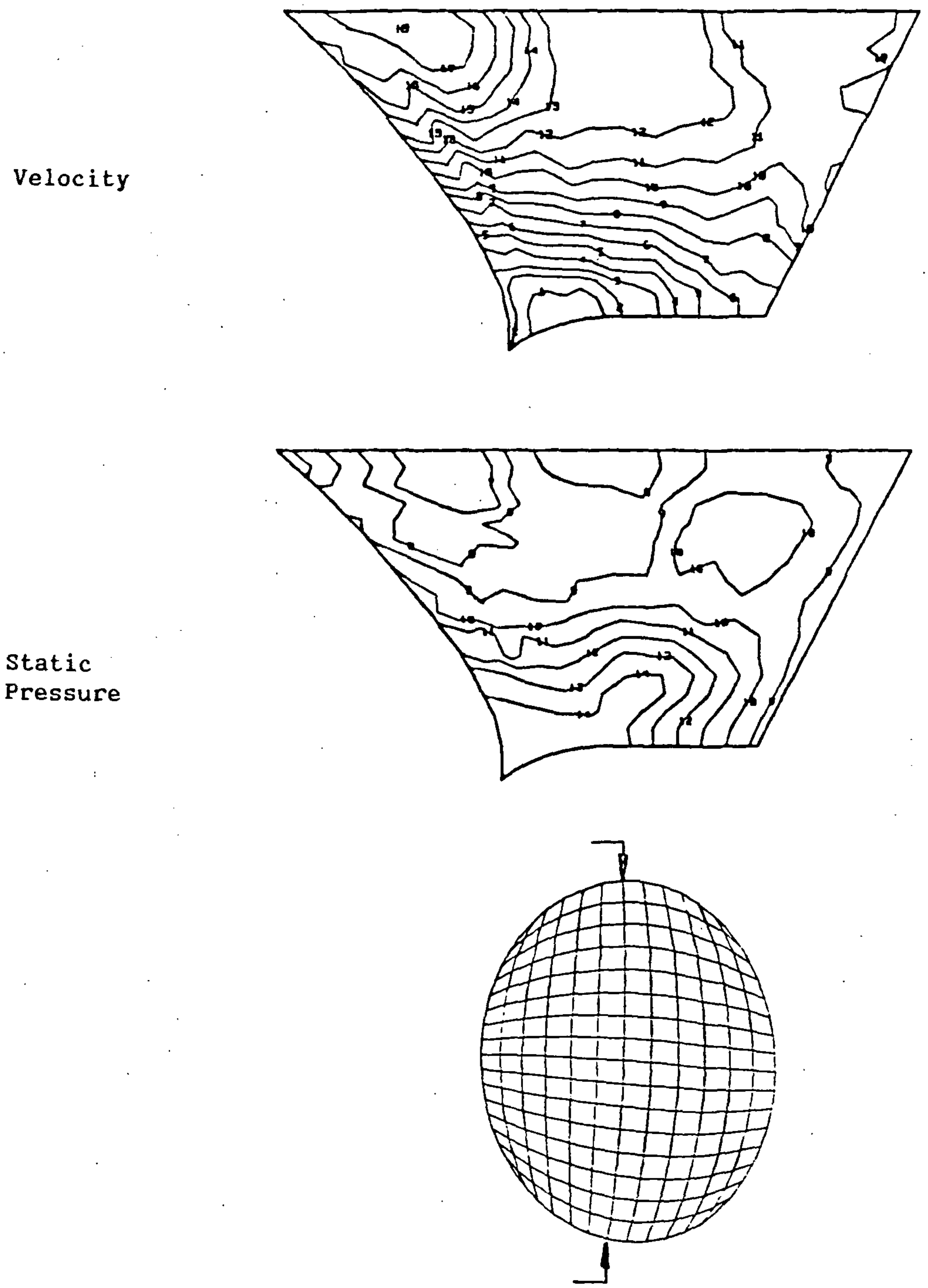

Fig. 28 Velocity Contours (Top) and Static Pressure Contours for the yz-Midplane of the Transfer Duct (Velocity Range is 20 - 360 ft/sec and Pressure Range is 180 - 184 psi)

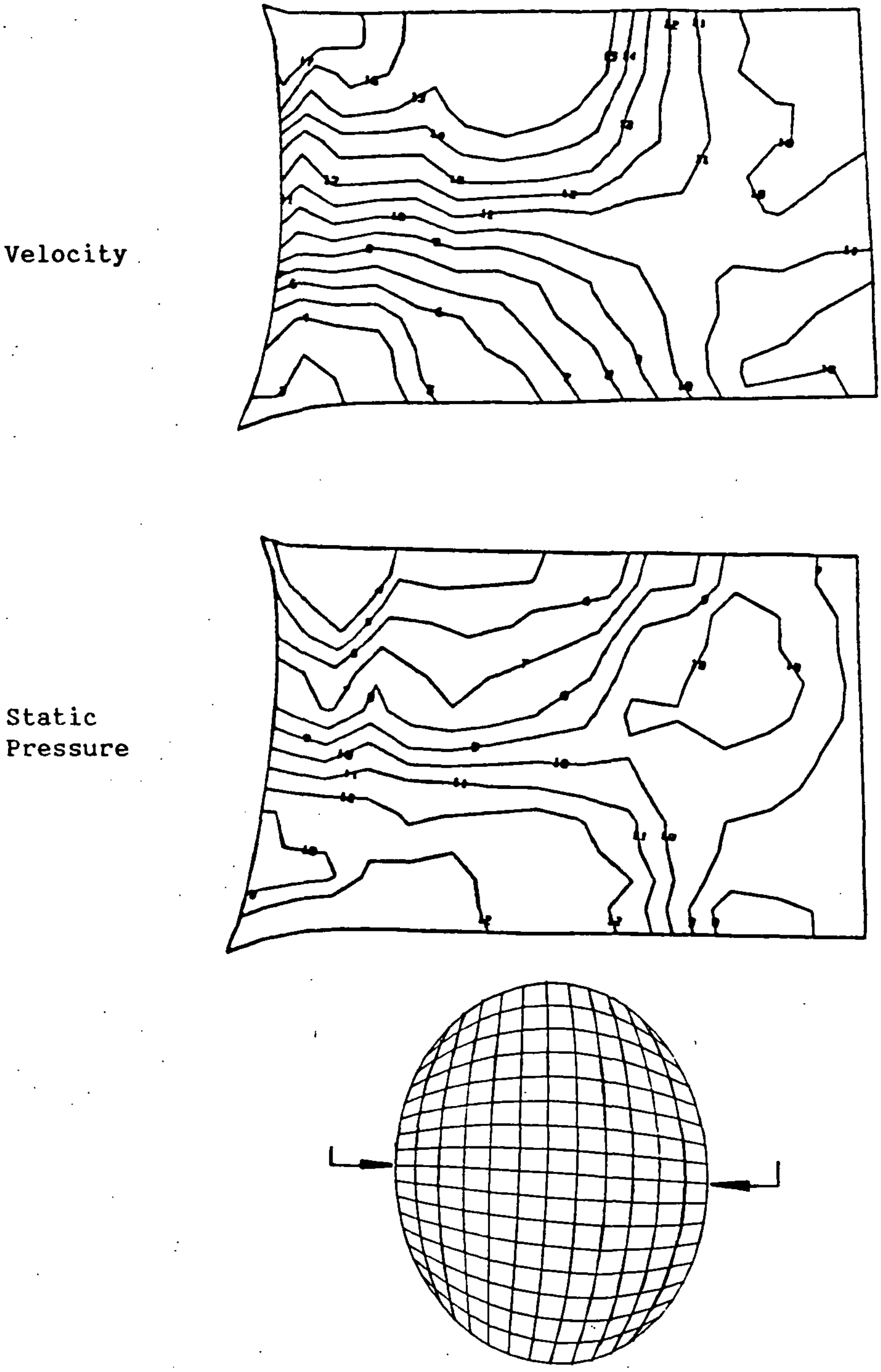

Fig. 29 Velocity Contours (Top) and Static Pressure Contours for the xz-Midplane of the Transfer Duct (Velocity Range is 60 - 340 ft/sec and Pressure Range is 177.8 - 184 psi)

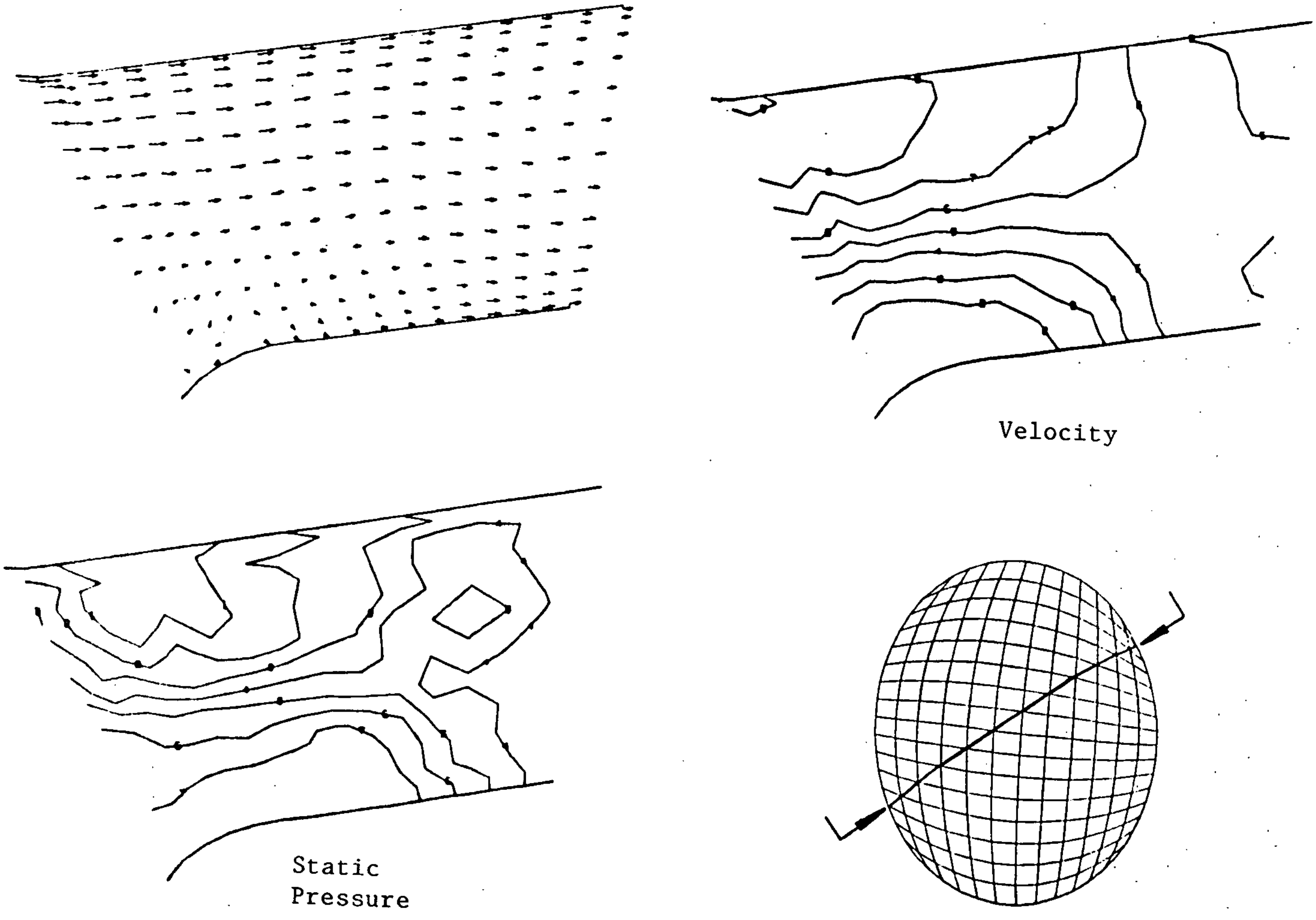

Fig. 30 Velocity Vectors, Velocity Contours, and Static Pressure Contours (Bottom) for a Diagonal View in the Transfer Duct (Plane and Orientation are Indicated in Lower Right. Velocity Range is 80 - 360 ft/sec and Pressure Range is 179.2 - 184.2 psi)

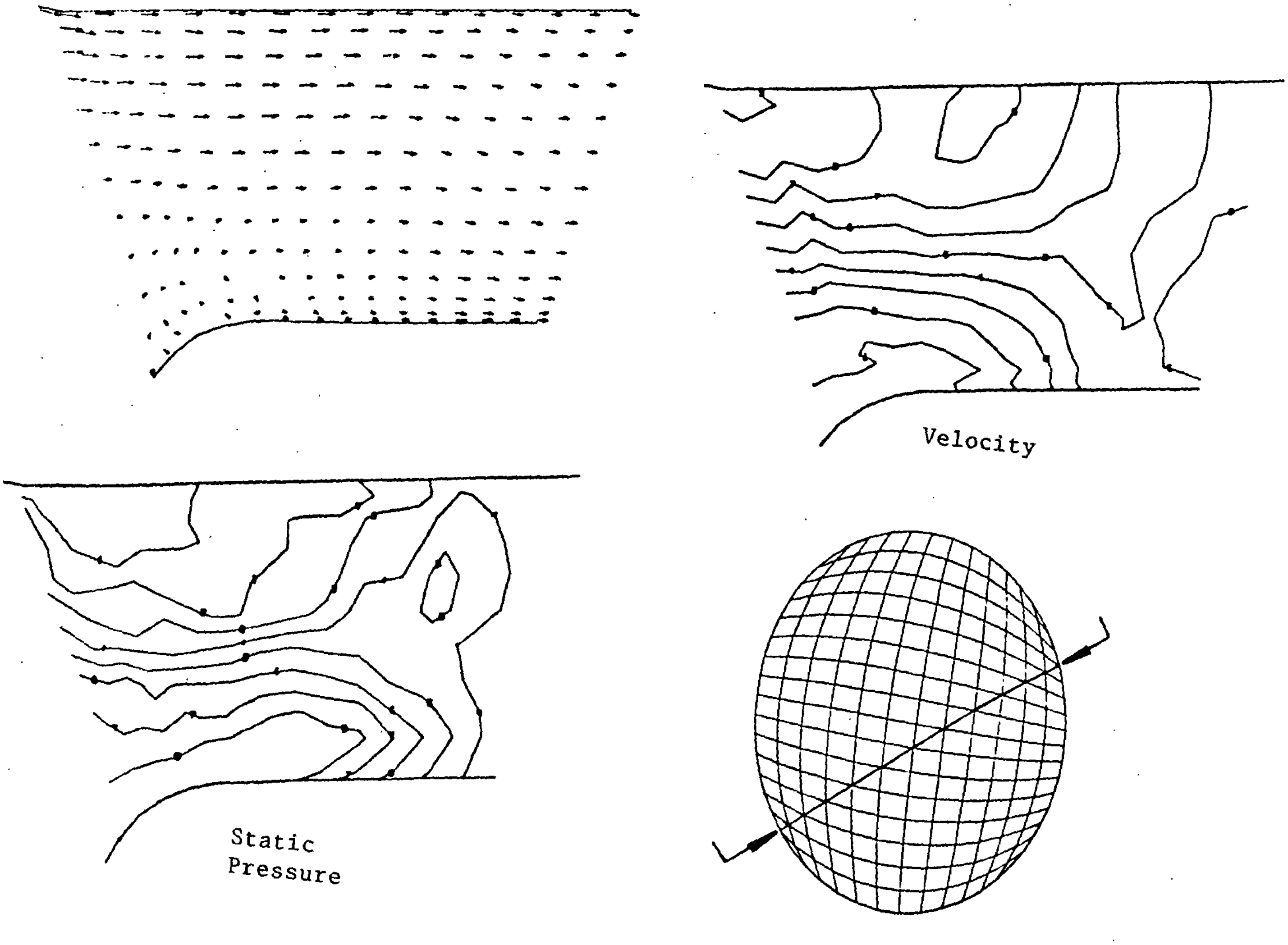

Fig. 31 Velocity Vectors, Velocity Contours, and Static Pressure Contours (Bottom) for a Diagonal View in the Transfer Duct (Plane and Orientation are Indiated in Lower Right. Velocity Range is 40 - 360 ft/sec and Pressure Range is 179.2 - 184.2 psi.)

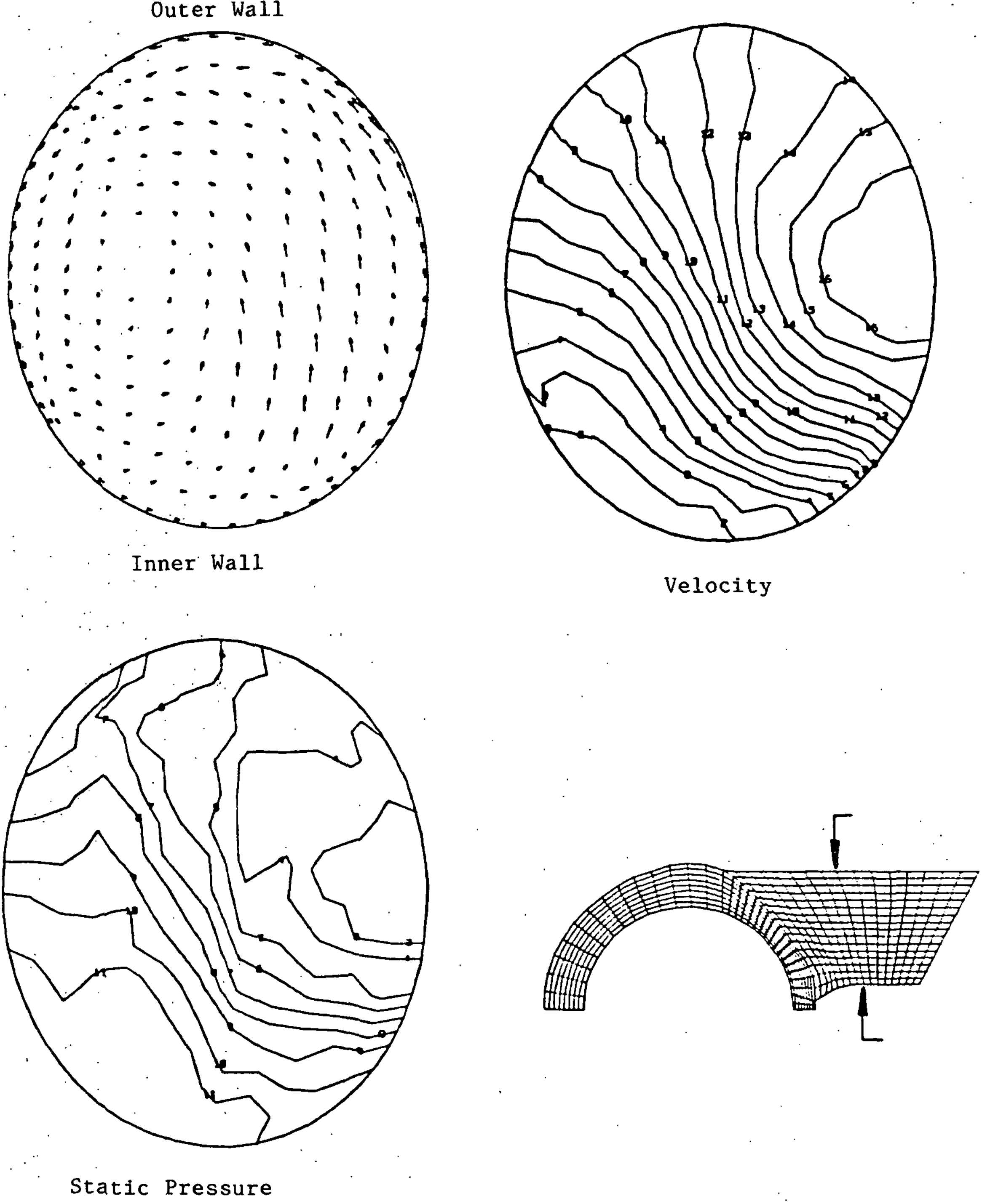

Fig. 32 Velocity Vectors, Velocity Contours, and Pressure Contours (Bottom) for a Central Cross Section of Transfer Duct (View is Looking into Bowl. Velocity Range is 40 - 320 ft/sec and Pressure Range is 179.2 - 184 psi.)

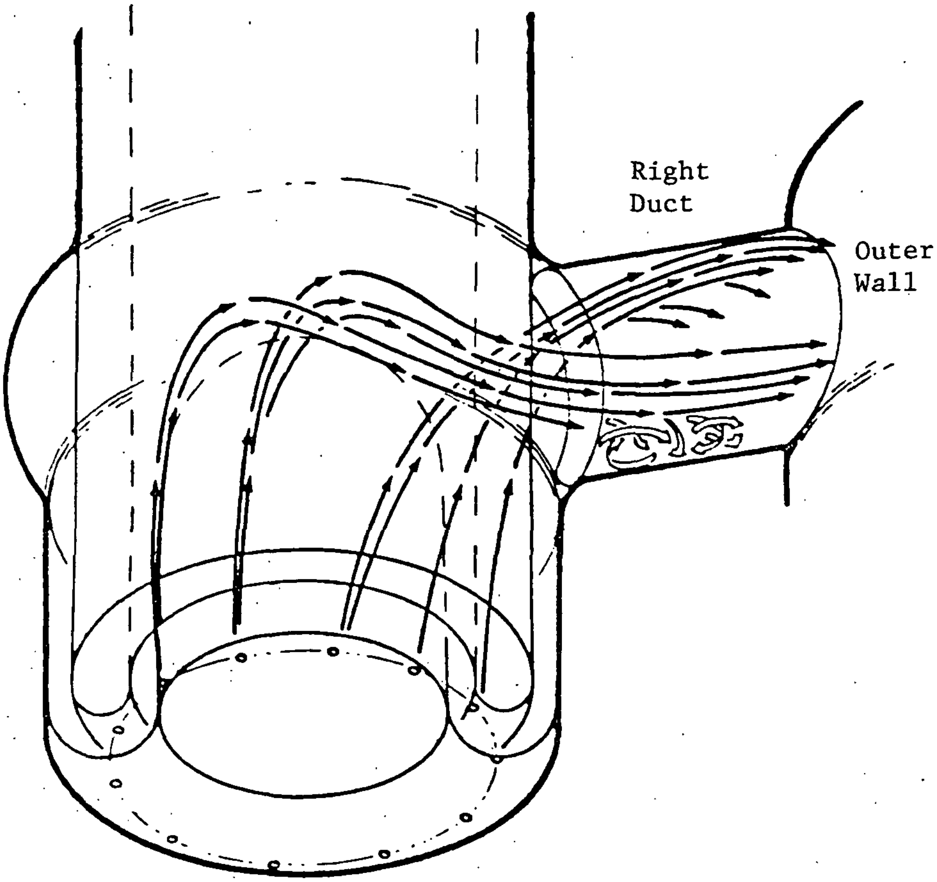

Fig. 33 Flow Features Observed in Flow Visualization Experiments Performed in a Water Flow Facility at NASA-MSFC

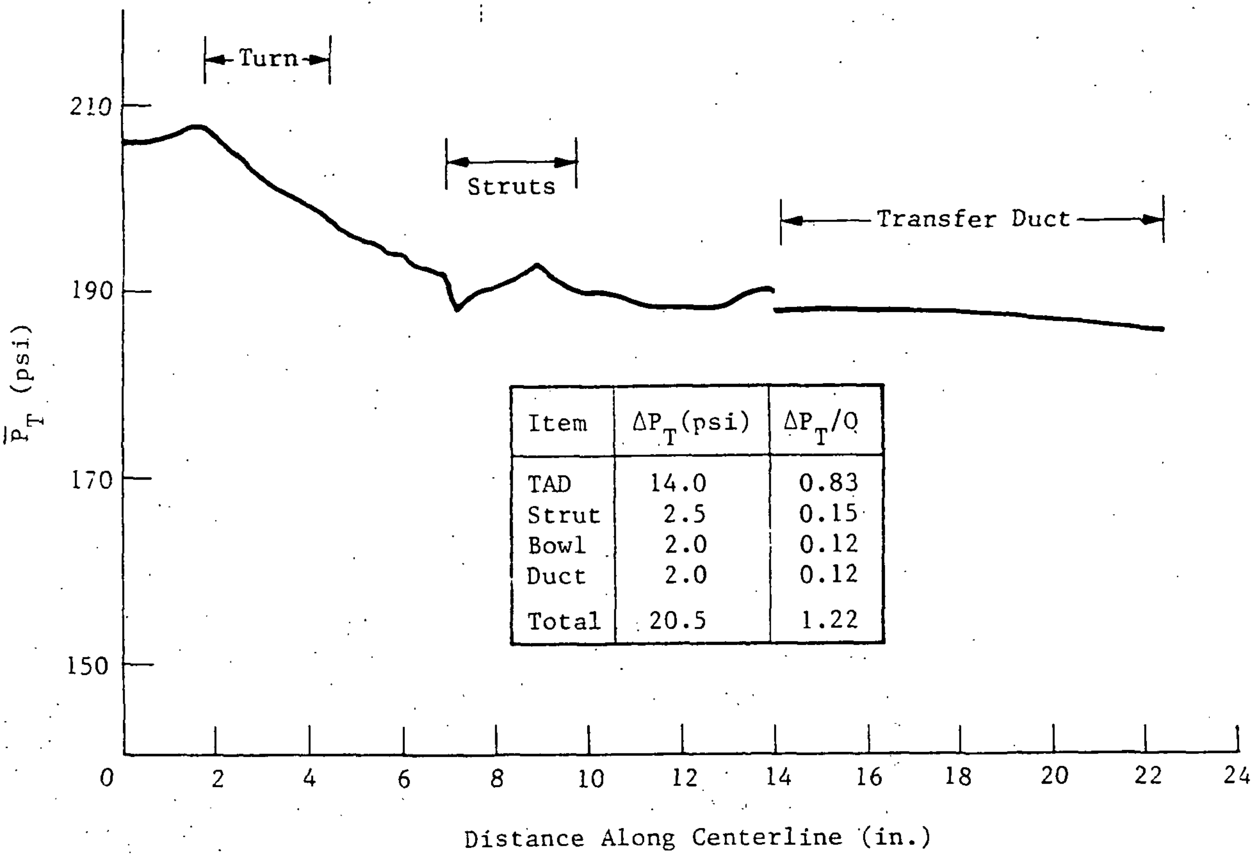

Item	ΔP_T(psi)	$\Delta P_T/Q$
TAD	14.0	0.83
Strut	2.5	0.15
Bowl	2.0	0.12
Duct	2.0	0.12
Total	20.5	1.22

AR-86-267

Fig. 34 Diagram if (a) Sudden Concentration and (b) Sudden Expansion for Flow in a Pipe. Values for ΔP are Those Determined for Total Pressure Loss on Entering and Learing the Strut Region of the Manifold.

Of major importance is the longitudinal distribution of the average total pressure through the manifold. As was done previously for the laminar computation the mass-averaged total pressure was determined and is plotted in Fig. 34. For direct comparison the same pressure range as in the laminar case was used on the vertical axis. As expected the largest pressure drop occurs in the TAD (68 percent). Because of the coarseness of the computational grid in the region of the struts an oscillation appears in the pressure distribution. The difference between the total pressure before and after the struts is 2.5 psi. Due to the pressure oscillation through the strut region the relevance of this value is in question. One can, however, obtain a reasonable estimate of this pressure loss by dividing it into three parts: losses due to a sudden contraction, flow in a channel, and a sudden expansion; and making an estimate of each part.

For the losses due to entering and exiting the struts we use commonly employed relationships for sudden contractions and expansions in pipe flow. The decrease in pressure, ΔP, in each case can be written as

$$\Delta P = K \frac{1}{2} \rho V^2, \qquad (12)$$

where K is called the loss coefficient and $\frac{1}{2}\rho V^2$ is the average dynamic pressure in the region of smaller cross section. In both instances the loss coefficient depends on the ratio of the cross-sectional areas (see Fig. 35). For an expansion K can be estimated using (Ref 8)

$$K_{exp} = \left(1 - \frac{A_1}{A_2}\right)^2, \qquad (13)$$

and for a contraction empirical results for losses in reducing bushings can be used. Equation (13) can be derived by combining the momentum equation, a modified Bernoulli equation which includes the loss tern given by Eq. (12), and the continuity equation to the one-dimensional flow shown in Fig. 35b.

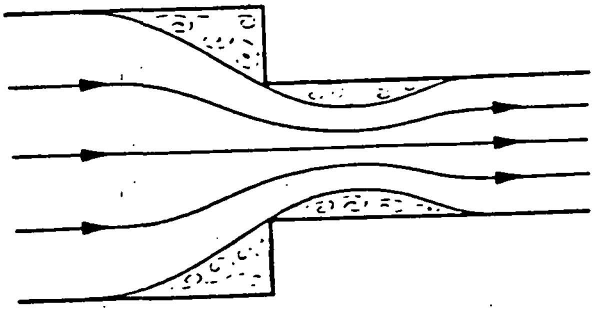

a. ΔP = 0.87 psi

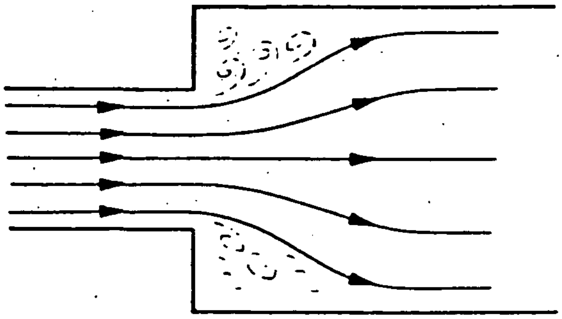

b. ΔP = 1.09 psi

Fig. 35 Loss Coefficients for Entering and Exiting Struts

Using the actual physical dimensions of the manifold we obtain for the cross-sectional areas before, in, and just after the strut region: 0.30 ft^2, 0.27 ft^2 and 0.38 ft^2, respectively. Substituting the appropriate value into Eq. (13) yields a value for the expansion loss coefficient of 0.088. The area ratio for the contraction is 0.90. This value can be used to estimate the contraction loss coefficient from a graph of empirical results for pipe flow given by Jana (Ref. 7) From this source we obtain a value of 0.07. The average dynamic pressure in the strut region can be estimated from the area ratio between the TAD inlet and the strut channel cross section and the average dynamic pressure at the TAD inlet. The mass-averaged dynamic pressure at the TAD inlet is 16.81 psi. Using the ratio of TAD inlet area to strut channel area of 0.86 we find 12.4 psi to be the estimate of the dynamic pressure in the strut channels. Equation (12) can now be used to find the estimate of the contraction pressure drop to be 0.87 psi and the estimate of the expansion pressure drop to be 1.09 psi.

To obtain an estimate of the pressure drop for flow in the strut channels we use the equation (Ref. 9)

$$\Delta P = f\ 1/2\rho V^2 \frac{\Delta x}{D} , \tag{14}$$

where D is a hydraulic diameter equal to four times the cross-sectional area divided by the wetted perimeter, Δx is the length of the struts (1.03 inches), and f is a friction coefficient for turbulent channel flow given by

$$f = 0.495\ (\log Re)^{-2.2} , \tag{15}$$

and where the Reynolds number, Re, is based on the dimension, D. Employing actual strut dimensions D is found to be 0.0463 ft. From the previously estimated dynamic pressure value in the strut channel we find, using Eq. (14), that the pressure loss estimate for flow there is 0.22 psi.

Summing all three estimated pressure loss components for flow through the strut region we get 2.2 psi. This compares well to the 2.5 psi obtained in the numerical computation, even though the struts were not well modeled.

Air flow measurements by Rocketdyne (Ref. 10) using the HGM II^+ geometry show an average total pressure loss from a position just downstream of the 180 deg. turn in the TAD to the transfer duct exit to be 9.48 psi. Relative to the measured average dynamic pressure at the TAD inlet (the turbine exit) of 11.122 psi, this provides a total pressure loss coefficient C_p of 0.85. Using the computed results plotted in Fig. 34 between the same two positions we find a C_p value of 0.71. These two values compare favorably. An experimental value for total pressure at the turbine exit was not provided, hence a comparison with the measured net C_p is not possible.

Further comparison of computational results to air flow measurements by Rocketdyne are shown in Figs. 36 and 37. Both figures display the circumferential static pressure distribution at the outer wall of the manifold. Figure 36 is for a position just downstream of the turn in the TAD, and Fig. 37 is for a position just after the struts at the entrance of the bowl. The apparent oscillations appearing in the computational results are due to the coarseness of the grid used. In both figures the experimental data displays some minor asymmetries which can not be predicted by the computations. A major disagreement between computation and experiment occurs in Fig. 36 at the circumferential position of 90- and 270-deg where experiment indicates a position of almost maximum static pressure. This would correspond to a position of minimum flow speed which both computations predict to be near the 180-deg position. Except for this disagreement the turbulent results agree more closely with the measurements. The laminar results predict too wide a variation between maximum and minimum pressures at this location. In Fig. 37 good agreement is found between computational and experimental results.

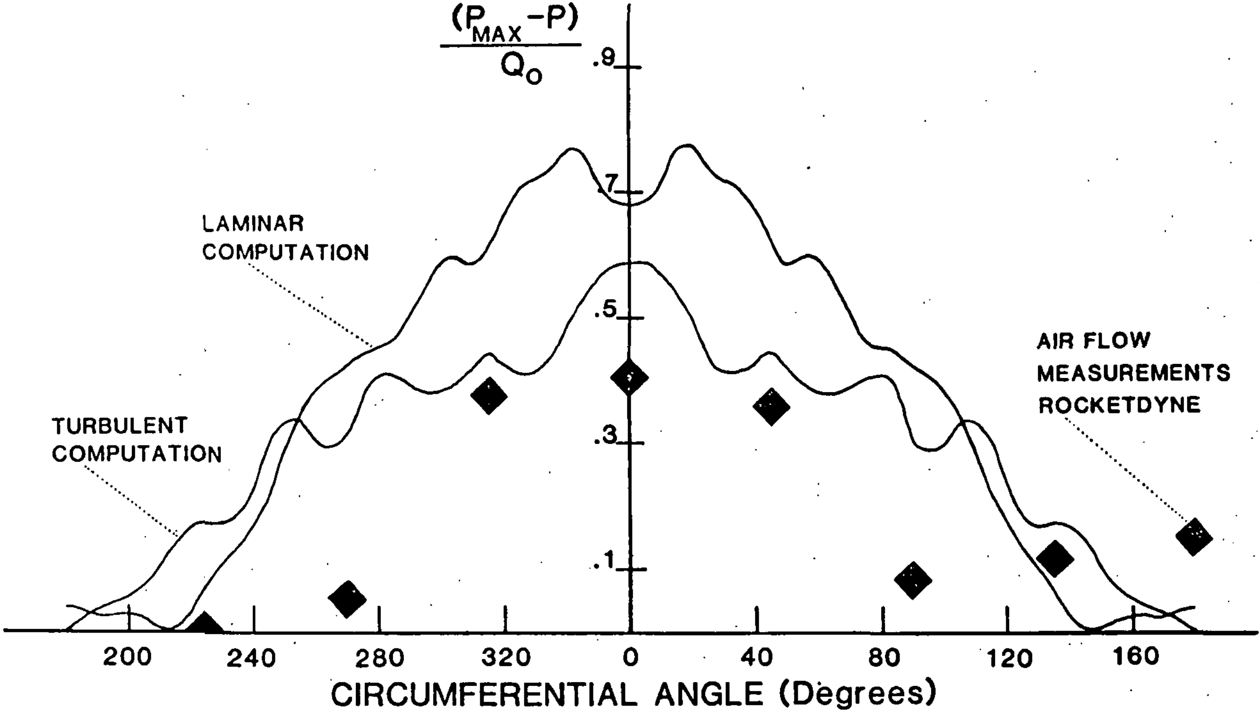

Fig. 36 Circumferential Static Pressure Distribution Just Past Turn in TAD

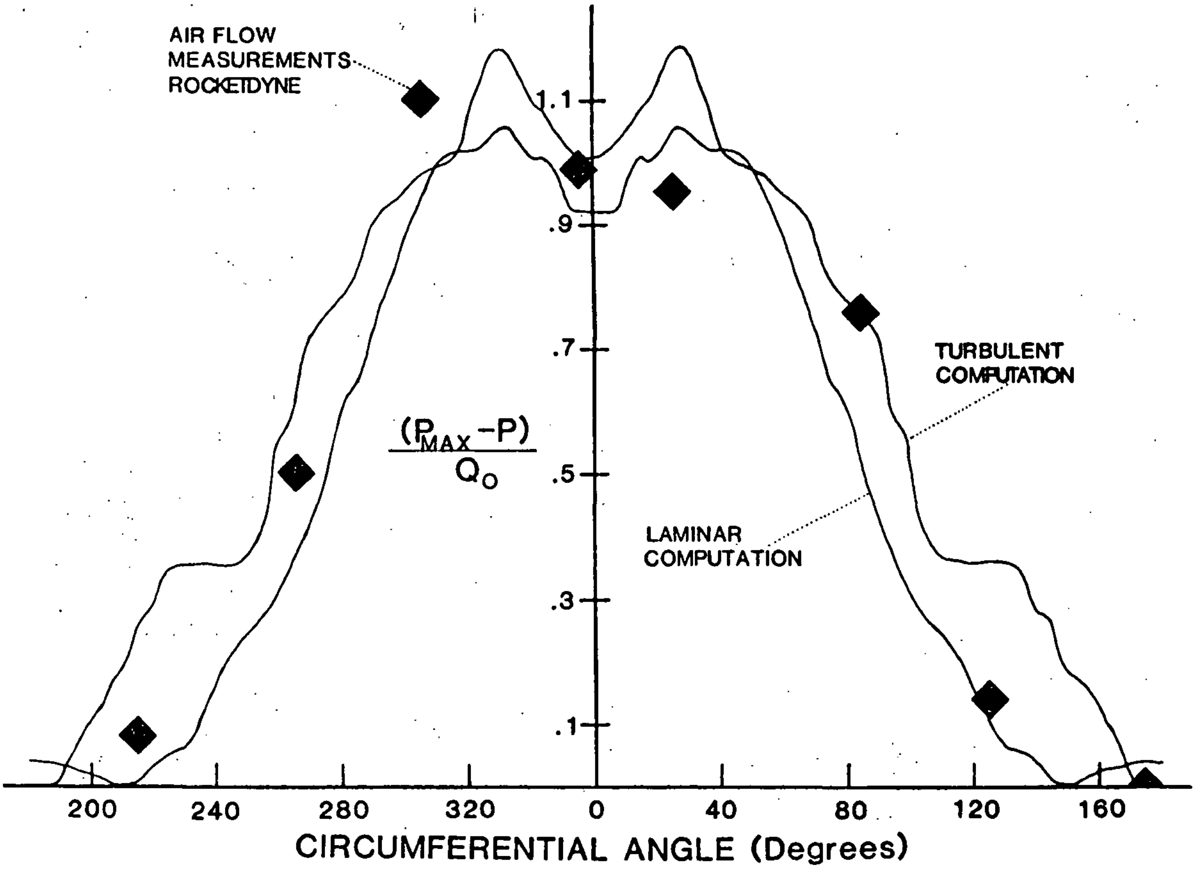

Fig. 37 Circumferential Static Pressure Distribution Just Past Struts at Entrance to Bowl

4. CONCLUDING REMARKS

Several observations can be made based on the results of the computational simulation of turbulent flow in the SSME HGM II^+ geometry herein presented. Air flow measurements (Ref. 10) indicate a region of separation on the inside wall of the TAD just downstream of 180-deg turn. Flow visualization studies in a water flow facility (Ref. 7) show a region of recirculation in the back of the bowl just opposite the transfer ducts. The absence of these two flow features from numerical results can be attributed directly to the coarseness of the computational grid employed in the calculation. It is also clear that the struts cannot be modeled well by such a coarse grid structure. However a region of recirculation and secondary flow swirl in the transfer duct observed in the flow visualization study (see Fig. 33) was predicted in the numerical results (see Figs. 30, 31 and 32). In addition, good agreement was found between results of air flow measurements for total pressure loss coefficient, from a position just downstream of the 180-deg turn in the TAD to the transfer tube exit, and the computed loss coefficient between the same two positions. Furthermore, computed circumferential static pressure distributions also compared well to air flow measurements at the same locations. Thus the combination of a coarse grid with a simple mixing length turbulence model employing a wall function can provide good predictions of total pressure losses and statiac pressure distributions for high Reynolds number internal flows in the complicated geometries of the SSME/HGM.

REFERENCES

1. Spradley, L.W., J.F. Stalnaker, M.A. Robinson, and K.E. Xiques, "Finite Element Algorithms for Compressible Flow Computation on a Supercomputer," in Finite Elements in Fluids, Vol. 6, Wiley, New York, 1985.

2. Prozan, R.J., L.W. Spradley, P.G. Anderson, and M.L. Pearson, "The General Interpolants Method," AIAA Paper 77-642, Albuquerque, June 1977.

3. See for example Computational Fluid Mechanics and Heat Transfer, by Anderson, Tannehill, and Pletcher, McGraw-Hill, New York, 1984, p. 190.

4. Pelaccio, Dennis G., "Duct Flow Nonuniformities Study," Final Report RI/RD83-160, Rockwell International, Rocketdyne Division, 30 June 1983.

5. See for example Boundary Layer Theory, by Schlichting, McGraw-Hill, New York, 1968, p. 551.

6. Ibid., p.568.

7. Wiegman, B., J. Heaman, and P. Ramsey, "Water Flow Visualization Results on a Phase III, One-Half Scale, SSME Hot Gas Manifold (HGM) with Sharp Corner Transfer Duct Inlets", CFD Workshop, NASA-Marshall Space Flight Center, 28-30 November 1984.

8. Introduction to Fluid Mechanics, by W.S. Janna, Brooks/Cole Engineering Division, Wadswaith, Inc., Monterey, Calif., 1983, p. 171-175.

9. Viscous Fluid Flow, by Frank M. White, McGraw-Hill, New York, 1974, p. 486-488.

10. O'Connor, George, and Winston M. Cuan, (Rockwell International Corp., Rocketdyne Division), Private Communications.

Appendix

COMPUTATION BACKGROUND
DATA SUMMARY

Appendix

Boundary Conditions (Laminar and Turbulent)

At TAD inlet plane: Total pressure held constantly, y- and z-components of velocity fixed at zero, direction of x-component of velocity held fixed.

At transfer duct exit plane: Static pressure held constant.

Initial Conditions

Pressure: Both computations were started with a circumferential static pressure variation with TAD and bowl given by Eq. (3). A total pressure drop from inlet to exit planes was initialized at five percent for the turbulent case and fifteen percent for the laminar case. At the inlet plane the total pressure for the turbulent and laminar cases was 206.3 psi and 204.1 psi, respectively. The corresponding initial static pressures were 191.4 psi and 194.4 psi.

Velocity: Both computations were started with a circumferential velocity variation at the inlet plane given by Eq. (4). The initial average speed at the inlet plane for both cases was approximately 380 ft/sec which gave an initial mass flow rate for both of approximately 36 lbm/sec. The flow speed through the system was initialized for constant mass flow.

Problem Parameters

Governing Equations: An explicit predictor-corrector finite difference algorithm was used to solve the continuity and momentum equations. An isothermal equation of state with an artificial compressibility was employed to obtain the pressure from the density.

Mass/Flow Rate: At convergence the mass flow rates for the turbulent and laminar cases were 42.5 lbm/sec and 30.1 lbm/sec, respectively.

Reynolds Number: Based on the channel width at TAD inlet, final averaged speeds at that location, and the laminar viscosity employed, the Reynolds Numbers for the turbulent and laminar cases were 2.5×10^6 and 263, respectively.

Mach Number: Based on a sound speed of 1200 ft/sec the maximum Mach Numbers in the flow fields were 0.49 for the turbulent case and 0.36 for the laminar case.

Turbulence Model

A simple Prandtl-Van Driest mixing length model was used in which the turbulent eddy viscosity depends on the local values of vorticity and mixing length.

By employing a basic high Reynolds Number than boundary layer logarithmic profile wall function expression we obtain a friction velocity, from which the shear stress on the wall was calculated.

Geometry Characteristics

The basic HGMII$^+$ geometry was modeled with a relatively coarse grid for both computations. Elliptical transfer duct-bowl intersections were smooth and rounded. With only minor variations exact dimensions were used from turbine exit to transfer duct exit. Struts at TAD exit were modeled in the turbulent case only.

Computational Grid

Total number of nodes were: 21,059 for turbulent and 33,524 for laminar.

In each section:	laminar	turbulent
	TAD - 18,963	TAD - 10,098
	Bowl - 11,025	Bowl - 7,425
	TD - 3536	TD - 3536

In both cases the number of nodes from inner to outer wall in TAD and Bowl was 9. No attempt was made to resolve boundary layers.

Computation Factors

Iterations: The number of explicit numerical iterations (one predictor-corrector sequence at each node) was 37,000 for the turbulent computation and 10,000 for the laminar computation.

Time Step: The time step corresponding to one iteration was 0.9×10^{-6} sec and 0.9×10^{-7} sec for the laminar and turbulent cases, respectively.

CPU Time: The CPU time per iteration per node for both computations was 6×10^{-5} sec. The total CPU time for the turbulent and laminar cases was 13 hours and 5.6 hours, respectively.

Convergence Criteria

Convergence was judged on the tendency of the sum of squares of unsteady derivatives of conserved quantities to decrease and remain constant and on the tendency of the mass flow rate at the exit plane to reach a steady value. Sample curves are shown in Figs. A1 through A4.

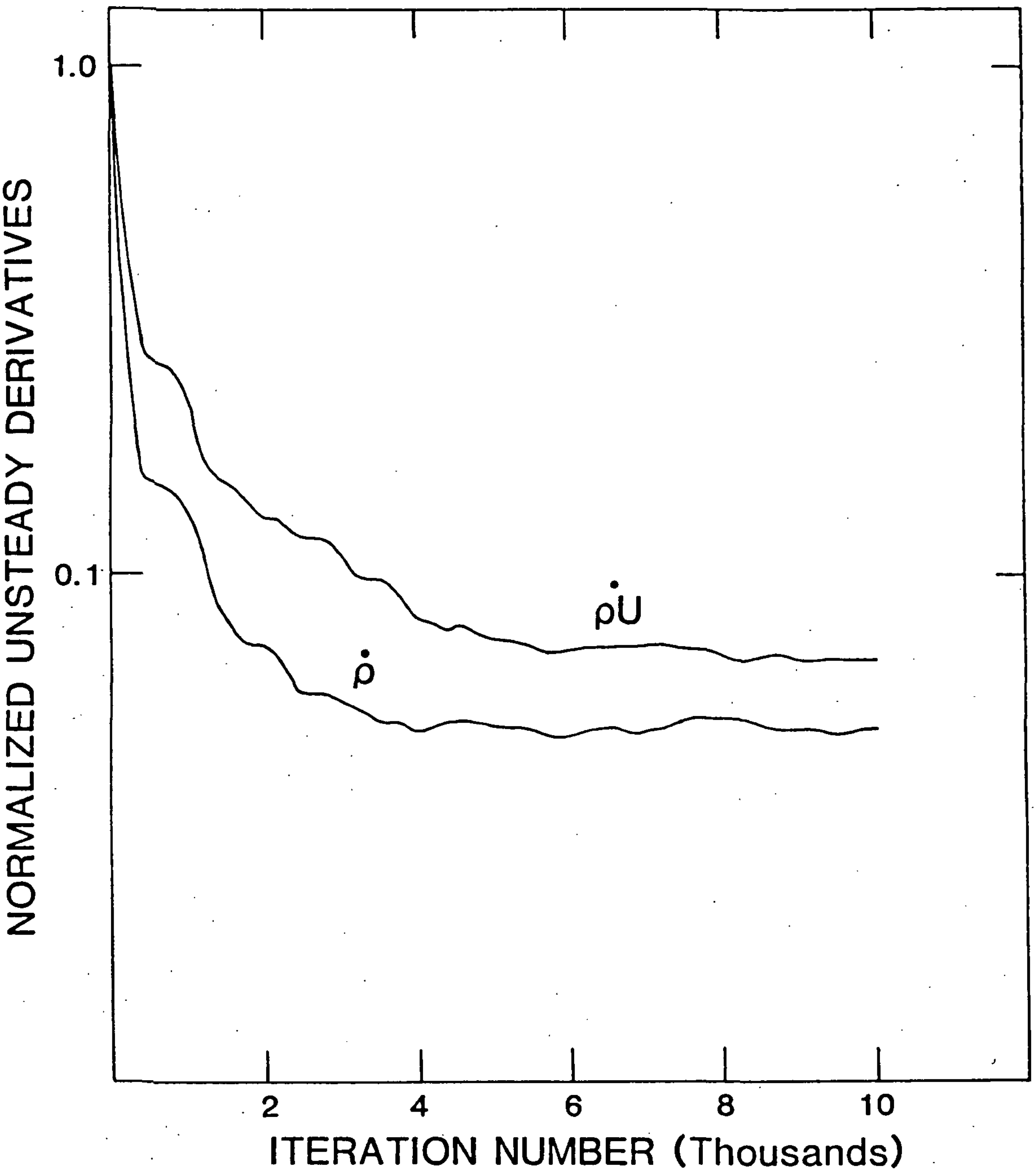

Fig. A1 Behavior of Unsteady Derivatives for the Laminar Computation

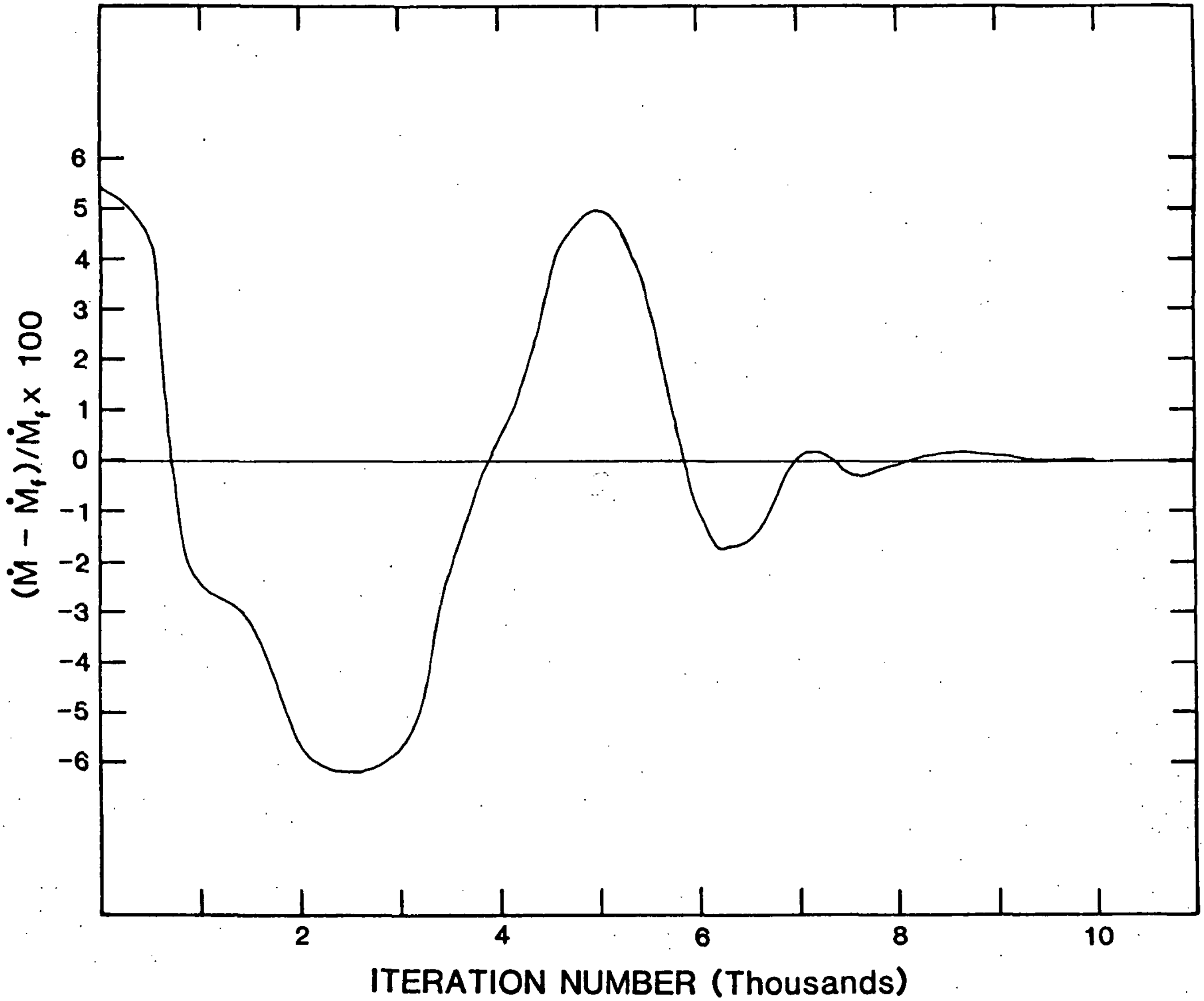

Fig. A2 Behavior of the Mass Flow Rate at the Exit Plane for the Laminar Computation (M_f is the final converged value.)

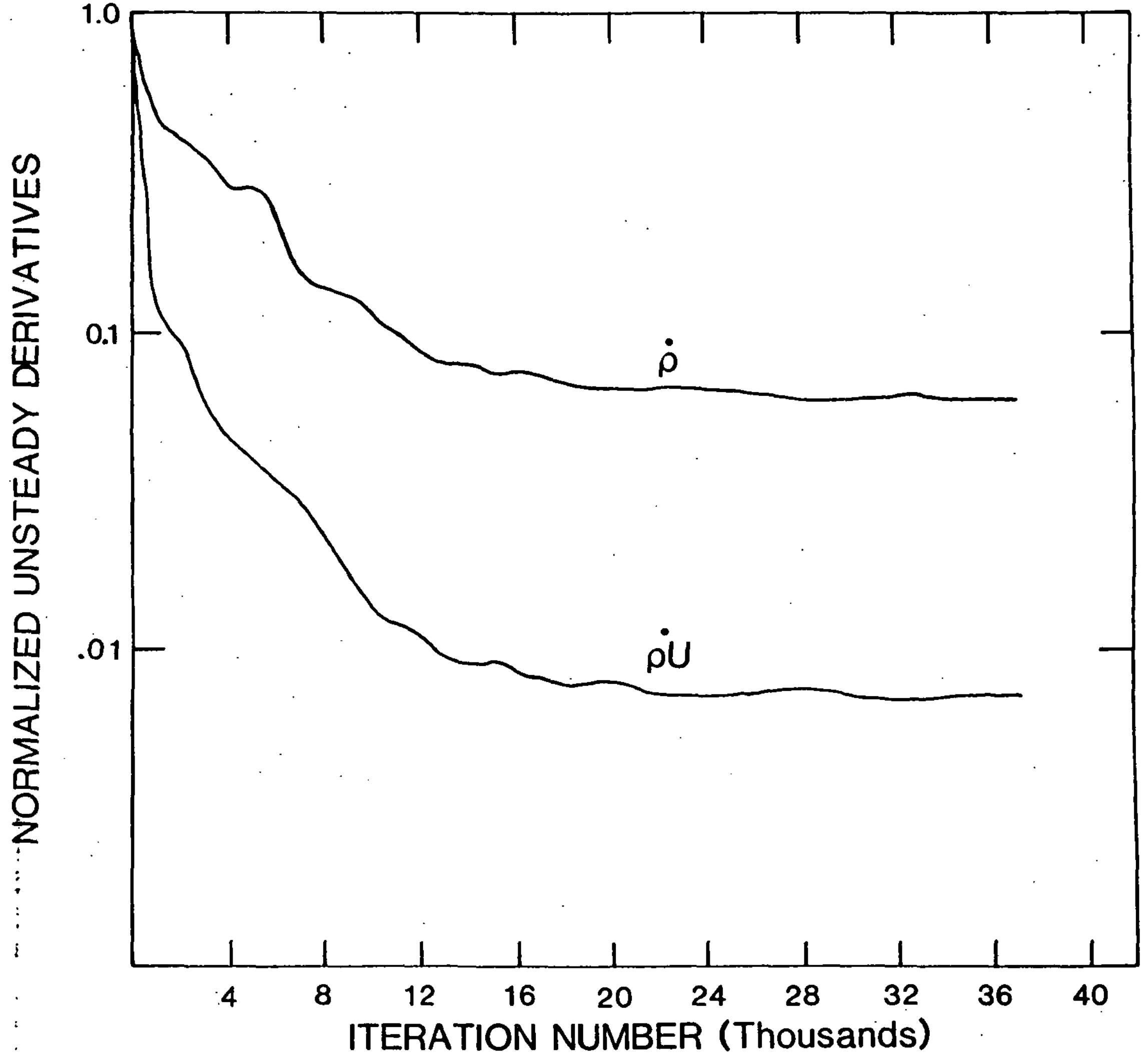

Fig. A3 Behavior of Unsteady Derivatives for the Turbulent Computation

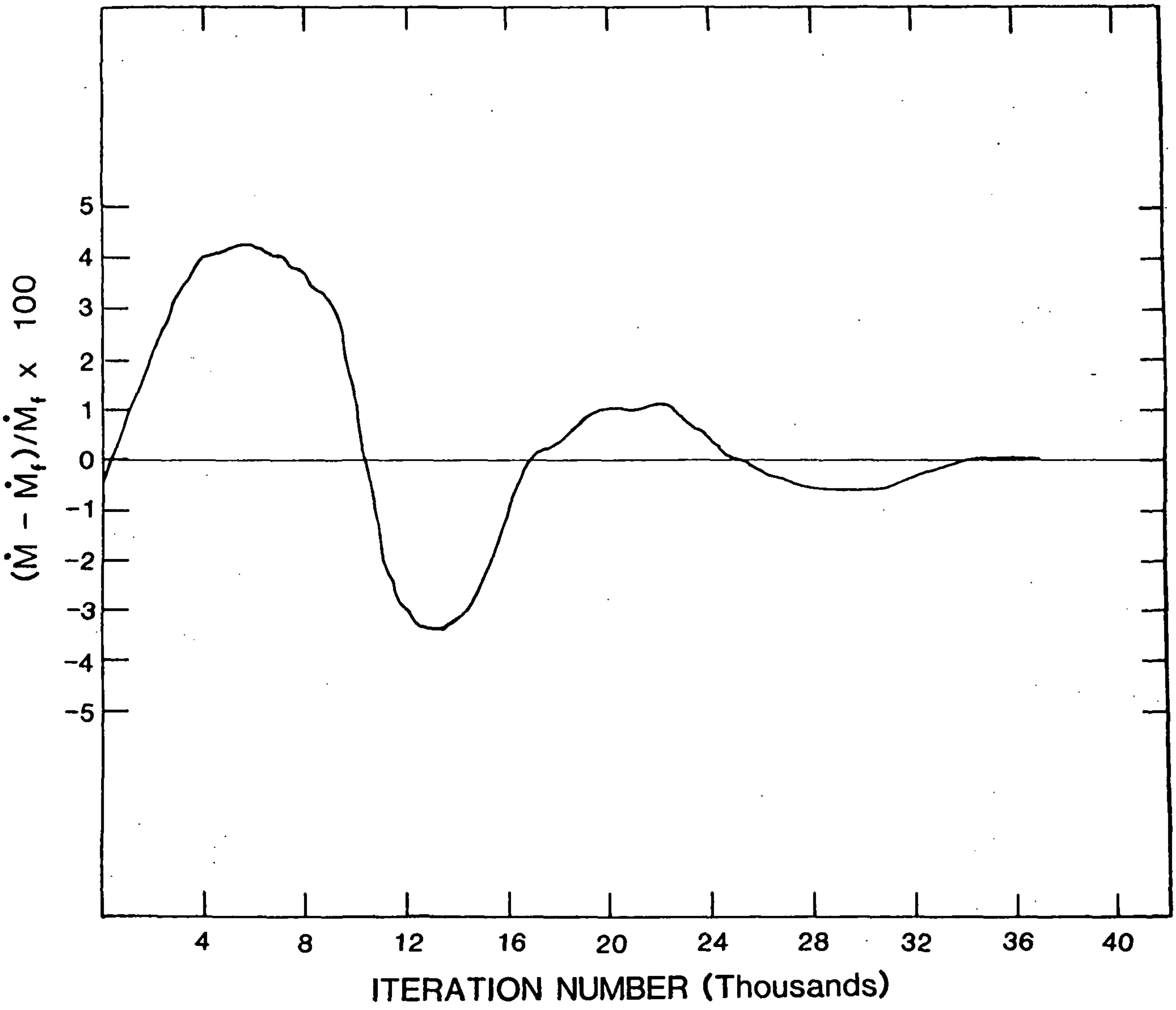

Fig. A4 Behavior of the Mass Flow Rates at the Exit Plane for the Turbulent Computation (M_f is the final converged value.)